Phase field modeling of dynamic fracture in elastoplastic composites with interfacial debonding

Pengfei Li, Yi Wu, Julien Yvonnet, Sili Liu, Shuitao Gu

▶ To cite this version:

Pengfei Li, Yi Wu, Julien Yvonnet, Sili Liu, Shuitao Gu. Phase field modeling of dynamic fracture in elastoplastic composites with interfacial debonding. Engineering Fracture Mechanics, In press. hal-04335588

HAL Id: hal-04335588
https://univ-eiffel.hal.science/hal-04335588v1

Submitted on 11 Dec 2023

Phase field modeling of dynamic fracture in elastoplastic composites with interfacial debonding

Pengfei Li[a], Yi Wu[b], Julien Yvonnet[c], Sili Liu[a], Shuitao Gu[d,*]

[a]*School of Civil Engineering, Jiangsu Open University, Nanjing, 210036, China*
[b]*School of Mechanical Engineering, University of Science and Technology Beijing, Beijing, 100083, China*
[c]*MSME, Univ Gustave Eiffel, CNRS UMR 8208, F-77454 Marne-la-Vallée, France*
[d]*School of Civil Engineering, Chongqing University, Chongqing 400044, China*

Abstract

In this work, we extend a phase field formulation for dynamic ductile fracture to consider interfacial debonding in elastoplastic composites. The interfacial weak zone is created through a regularization of the sharp interfaces, and the singular strain part along the interfaces is approximated by using a Taylor expansion. Then, a strain density depending on the displacement jump related to matrix/inclusions decohesion is added to the total energy to take into accout interfacial debonding. The coupling problems (displacement, plasticity and damage problems) are derived within the variational framework and a staggered iterative algorithmic procedure is described to solve the coupling problems. Numerical examples demonstrate that this method can handle the initiation, propagation, and interaction between bulk dynamic fracture and interface cracks, as well as the anisotropic behavior in the complex microstructure of elastic-plastic composite materials. It also indicates that this model is convergent in terms of mesh refinement.

Keywords: Phase field method, Dynamic fracture, Interfacial debonding, Elastoplastic composites, Image-based models

---

1. Introduction

The computational modeling of dynamic fracture in elastoplastic composites is of essential importance for a wide range of applications including automotive, electronics, aerospace, and biotechnology engineering, e.g. evaluations of fracture resistance of 3D printed short fiber reinforced composites used in aerospace (see e.g.[1, 2]), where components frequently suffer from dynamic loadings like wind, impact, and blast loads. In order to optimize dynamic fracture processing and evaluate dynamic fracture resistance, thereby maximizing the crack resistance of components, it is crucial to develop an efficient and robust numerical method for the modeling of the dynamic fracture processing.

In the past decades, many models and numerical methods have been proposed to simulate dynamic crack propagation, which can be simply classified into two categories: discrete and continuous approaches. In the former, the displacement field is allowed to be discontinuous on the

---

[*] Corresponding author

Email address: `gust@cqu.edu.cn` (Shuitao Gu)

fracture surface, while in the latter, the displacements are continuous everywhere, but the stresses are gradually decreased to describe the degradation process using some softening material models. The well-known theories for the discrete approaches are the discrete elements [3, 4], peridynamics [5–7], cohesive models [8–10], and the extended finite element method (XFEM) [11–13]. Continuum damage mechanics is probably the most widely used theory categorized in the continuous fracture approach [14, 15].

From a computational perspective, most of the above mentioned approaches suffer in situations with complex crack patterns including branching, giving substantial difficulties in numerical implementations, and often restrict the above formulations to simple crack pattern. This difficulty can be overcome by the variational approach to fracture [16–21], also called phase field method in the literature, which regularizes sharp crack discontinuities within a pure continuum formulation, and offers several advantages, such as the possibility to initiate fracture from undamaged zones, to handle arbitrary fracture patterns without specific treatment and use of classical finite elements, a variational framework allowing to involve many models or mechanisms, and a mesh-independence due to a gradient description of damage. Detailed information for the phase field method can be found e.g. in the review papers [20, 22].

Phase field method has been recently extended to ductile fracture behaviors by coupling gradient damage mechanics with models of elasto-plasticity. These models can be simply classified into two families: weak coupling and strong coupling models. A well-known weak coupling model was proposed in Ambati et al. [23], where a characteristic degradation function that couples damage to plasticity in a multiplicative format is used. Another typical weak coupling model, one can refer to [24], where the coupling is based on a hardening degradation function related to the equivalent plastic strain which works on the initial fracture toughness. The above mentioned models, in spite of losing the variational consistance, can well simulate the ductile fracture in elastoplastic solids (see [25]). The strong coupling models e.g. in the papers [26–29], through introducing a damage based plastic energy into the total energy, allow the plastic energy to induce the crack initiation and propagation. The strong coupling models follow the variational framework and allow to include many models or mechanisms. Extensions of the strong coupling model to gradient plasticity at finite strains were considered in [30–33] based on a rigorous variational principle. A comparative study for different phase field models of fracture coupled with plasticity was outlined in [34].

With respect to dynamic fracture, phase field models have been considered in [19, 35–40], just to name a few. These models are based on the assumption that the kinetic energy is not affected by the phase field and the fracture energy is independent of the crack velocity. The dynamic crack branching phenomenon experimentally observed can be captured and mesh independent fracture energies were obtained e.g. in [41]. Currently, most of these works focused on the numerical simulation of the dynamic crack networks whereas Bleyer et al. [38, 42] presented some explanations of dynamic fracture behavior.

More recently, phase field method has been extended to the coupling of ductile and dynamic to simulate the dynamic crack initiation and propagation in elastoplastic solids. In [43] modeling of dynamic fracture in the logarithmic Lagrangian strain space has been presented with emphasis on analysing the transition of brittle-to-ductile failure mode. In [44], Molnár et al. proposed a robust and versatile open-source Abaqus subroutine for practical engineers as well as research scientists in a widely available commercial finite element code, which can be employed to study both brittle and ductile static and dynamic fracture. To this end, Wu and Shen [45] proposed a new phase field model for dynamic fracture in elastoplastic solids, which is achieved through the use of new plastic degradation function that allows for a transition between two dissipative stages.

In most of the above mentioned approaches, interfacial contributions were not included in the constitutive formulation, despite the fact that interfaces in composites may introduce additional weak zones and can strongly affect the damage mechanisms. In this respect, Paggi et al. [46] presented a novel combined approach that employs the phase field model to handle bulk brittle fracture and simulates interface debonding using classical cohesive elements. Msekh et al. [47, 48] applied the phase field approach to simulate progressive failure in polymer-matrix composites. Hansen-Dörr et al. [49] proposed a phase field approach to simulate interface failure between two dissimilar materials. In [50, 51], a simple framework that extends phase field to consider interfacial debonding has been proposed, where a regularized description of the sharp interface and displacement jumps around the interface has been used, and different damage behavior to the bulk and to the interface in the energy is associated with an appropriate weighting of indicator functions.

In this work, we propose an extension of the phase field model as presented in [44] for the simualtion of dynamic fracture in elastoplastic composites. The involved extensions comprise: (i) considering interfacial debonding between the inclusions and the matrix; (ii) modeling interactions between interfacial debonding and bulk dynamic ductile fracture; (iii) handling elastoplastic composite microstructures obtained from X-ray computed tomography (XRCT) technique. The interfacial weak zone is created through a regularization of the sharp interfaces, and the singular strain part along the interfaces is approximated by using a Taylor expansion. Then, a strain density depending on the displacement jump related to matrix/inclusions decohesion is added to the total energy to take into accout interfacial debonding. To maintain the regularized property of the approximation, smooth indicator functions are employed to weight the different terms in the energy with respect to the vicinity of interfaces. Then, the coupling problems, involving displacement, plasticity and damage problems, are derived and a staggered iterative algorithmic procedure is described to solve the coupling problems.

The paper is structured as follows. In Section 2, we introduce a regularization of bulk crack, interfacial damage, displacement jump and plasticity. Section 3 provides the phase field modeling of dynamic fracturing with interfacial damage in elastoplastic composites. Section 4 provides the FEM discretization and the flowchart for the overall algorithm. Section 5 provides the numerical examples. Finally, conclusions are drawn in Section 6.

2. Regularization of discontinuities and plasticity

Consider an open domain $\Omega \subset \mathbb{R}^D$ with $D = 2, 3$, describing a heterogeneous body which contains internal interfaces between two elasto-plastic phases. The external boundary of Ω is denoted by $\partial\Omega \in \mathbb{R}^{D-1}$, composed of Dirichlet and Neumann parts, denoted by $\partial\Omega_u$ and $\partial\Omega_F$, $\partial\Omega = \partial\Omega_u \cup \partial\Omega_F$, $\partial\Omega_u \cap \partial\Omega_F = \emptyset$, where displacements and tractions are prescribed, respectively. During the loading, crack may propagate in the matrix and can pass through the interfaces, where the crack surface and the interfaces are collectively denoted by Γ and Γ^I (see Fig. 1a), respectively. In this work, we employ the framework presented in [18, 52] for a regularized representation of discontinuities and extension to interfaces as in [50]. In this regularized framework, the cracks are approximately represented by a scalar phase field $d\left(\mathbf{x}, t\right)$ (see Fig. 1b) and the interfaces by a fixed scalar function $\beta\left(\mathbf{x}\right)$ (see Fig. 1d), the plastic response is regularized by using a gradient plasticity formulation (see Fig. 1c), and the displacement jump around the interface is regularized by using a Taylor expansion (see Fig. 1e).

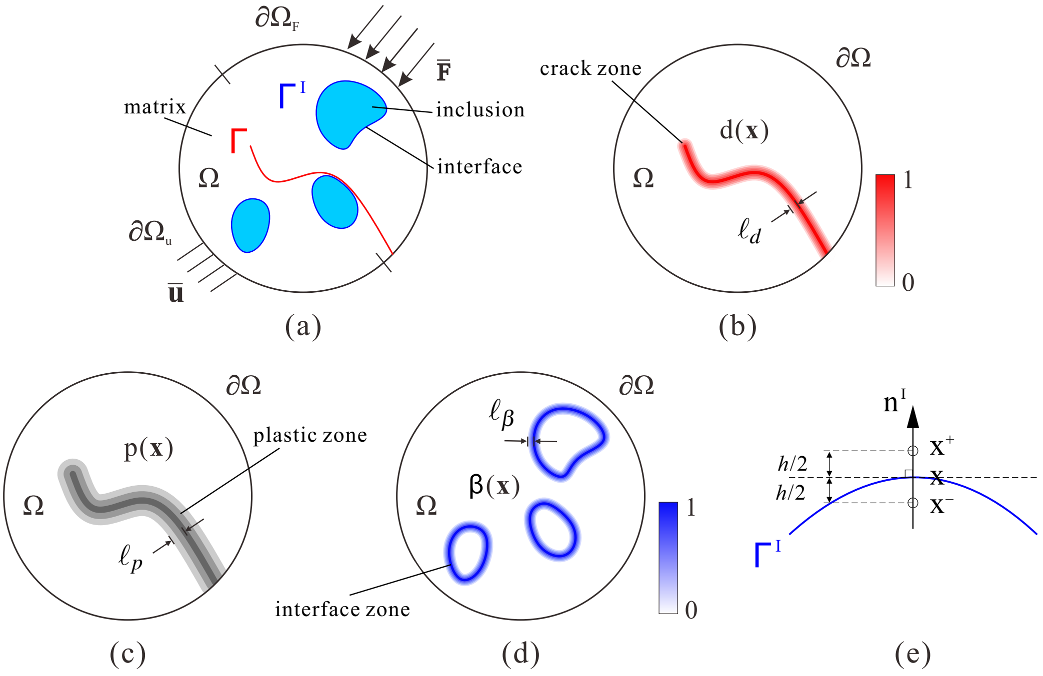

Figure 1: Regularization of discontinuities and plasticity: (a) a body containing sharp cracks and interfaces; (b) diffused approximation of cracks; (c) regularization of plastic response; (d) diffuse approximation of interfaces; (e) regularization of displacement jump.

2.1. Regularization of bulk cracks

For a known fixed crack surface Γ (see Fig. 1a), the scalar crack phase field $d\left(\mathbf{x},t\right)$ can be determined via solving the following boundary value problem (see [18] for more details):

$$\begin{cases} d\left(\mathbf{x},t\right)-\ell_d^2\Delta d\left(\mathbf{x},t\right)=0 \text{ in } \Omega, \\ d\left(\mathbf{x},t\right)=1 \text{ on } \Gamma, \\ \nabla d\left(\mathbf{x},t\right)\cdot\mathbf{n}=0 \text{ on } \partial\Omega, \end{cases} \tag{1}$$

where $\Delta\left(\cdot\right)$ and $\nabla\left(\cdot\right)$ are the Laplacian and gradient operator respectively, ℓ_d is a length scale parameter to govern the width of crack regularization zone and gives for $\ell_d\to 0$ the exact sharp crack as shown in Fig. 1b, $\mathbf{n}$ is the outward normal on $\partial\Omega$. It can be shown that (1) is the Euler-Lagrange equation for the following variational problem:

$$d=\operatorname{Arg}\left\{\inf_{d\in S_d}\Gamma^d\left(d\right)\right\},\quad \Gamma^d\left(d\right)=\int_\Omega\gamma_d\left(d\right)d\Omega,\quad S_d=\left\{d\mid d\left(\mathbf{x}\right)=1,\forall\mathbf{x}\in\Gamma\right\}, \tag{2}$$

where $\Gamma^d\left(d\right)$ represents the total length of the crack in 2D and the total crack surface area in 3D, and $\gamma_d\left(d\right)$ is the crack surface density function defined by:

$$\gamma_d\left(d\right)=\frac{d^2}{2\ell_d}+\frac{\ell_d}{2}\nabla d\cdot\nabla d, \tag{3}$$

where the second term in $\gamma_d(d)$ penalizes high values of $\nabla d(\mathbf{x})$ to prevent well-known related non-convergence issues with respect to the mesh discretization, which are found in local damage model.

2.2. Regularization of plasticity

With a similar manner, the plastic response can be regularized (see Fig. 1c) through introducing a gradient part into the initial plastic strain energy density function [30] as

$$\psi_0^p = \sigma_y p + \frac{1}{2} H p^2 + \frac{1}{2} \sigma_0 \ell_p^2 \nabla p \cdot \nabla p, \tag{4}$$

where σ_y and $H > 0$ are the yield stress and the hardening modulus parameters, σ_0 is a parameter to keep unit consistency for the gradient part and $\sigma_0 = 1$ MPa used in the following, p denotes an equivalent plastic strain described by the evolution equation

$$\dot{p} = \sqrt{\frac{2}{3}} \left\| \dot{\boldsymbol{\varepsilon}}^p \right\|, \tag{5}$$

where $\dot{(.)}$ is time derivative and $\boldsymbol{\varepsilon}^p$ is the plastic strain. In (4), ℓ_p is a plastic length scale related to a strain-gradient hardening effect and takes into account size effects to prevent the nonphysical mesh sensitivity of the localized plastic deformation in softening materials.

2.3. Regularization of interfaces

Similarily, the scalar interface function $\beta(\mathbf{x})$ can also be determined through solving the following boundary value problem

$$\begin{cases} \beta(\mathbf{x}) - \ell_\beta^2 \Delta \beta(\mathbf{x}) = 0 \text{ in } \Omega, \\ \beta(\mathbf{x}) = 1 \text{ on } \Gamma^I, \\ \nabla \beta(\mathbf{x}) \cdot \mathbf{n} = 0 \text{ on } \partial\Omega, \end{cases} \tag{6}$$

where ℓ_β is a length scale parameter to govern the width of the regularization zone of the interface and gives for $\ell_\beta \to 0$ the exact sharp interfaces as shown in Fig.1d. (6) corresponds to the Euler-Lagrange equation for the following variational problem

$$\beta = \mathrm{Arg}\left\{ \inf_{\beta \in S_\beta} \Gamma^\beta(\beta) \right\}, \quad \Gamma^\beta(\beta) = \int_\Omega \gamma_\beta(\beta)\, d\Omega, \quad S_\beta = \left\{ \beta \mid \beta(\mathbf{x}) = 1, \forall \mathbf{x} \in \Gamma^I \right\}, \tag{7}$$

where $\gamma_\beta(\beta)$ is defined by

$$\gamma_\beta(\beta) = \frac{\beta^2}{2\ell_\beta} + \frac{\ell_\beta}{2} \nabla \beta \cdot \nabla \beta. \tag{8}$$

2.4. Regularization of displacement jumps within interfaces

In the present work, a regularized approximation for the displacement jump $[\![\mathbf{u}]\!]$ is introduced to consider the interface debonding as presented in [50]. In order to derive a description of the displacement jump $[\![\mathbf{u}]\!]$, we first define the indicator function $\phi\left(\mathbf{x}\right)$ as

$$\phi\left(\mathbf{x}\right)=\beta\left(\mathbf{x}\right), \tag{9}$$

then the displacement jump $[\![\mathbf{u}]\!]$ can be regularized through using a Taylor expansion of the displacement field around a point $\mathbf{x}$ located on the interface (see Fig.1e)

$$[\![\mathbf{u}]\!]\simeq\mathbf{w}\left(\mathbf{x}\right)=\mathbf{u}\left(\mathbf{x}+\frac{h}{2}\mathbf{n}^I\right)-\mathbf{u}\left(\mathbf{x}-\frac{h}{2}\mathbf{n}^I\right)=h\nabla\left(\mathbf{u}\left(\mathbf{x}\right)\right)\mathbf{n}^I, \tag{10}$$

where $\mathbf{n}^I$ is the normal vector to Γ^I at the point $\mathbf{x}$ and is defined by:

$$\mathbf{n}^I=\frac{\nabla\phi\left(\mathbf{x}\right)}{\left\|\nabla\phi\left(\mathbf{x}\right)\right\|}, \tag{11}$$

$\mathbf{w}\left(\mathbf{x}\right)$ denotes the regularized displacement jump which is not only defined on the interface but over all the domain, and h is a small scalar parameter.

The traction acting on the interface oriented by $\mathbf{n}^I$ (see Fig. 1e) is defined by

$$\mathbf{t}\left(\mathbf{w}\right)=\frac{\partial\overline{\psi}^I\left(\mathbf{w}\right)}{\partial\mathbf{w}}, \tag{12}$$

where $\overline{\psi}^I$ is the interface strain density depending on the regularized displacement jump $\mathbf{w}$. Note that as discussed in [50], it is not required to introduce history variables into this formulation for the interfaces, and the diffuse damage field is used to describe the irreversibility of the interfacial debonding. For 2D problems, the traction $\mathbf{t}\left(\mathbf{w}\right)$ has the following form

$$\mathbf{t}\left(\mathbf{w}\right)=\left[t^n,t^t\right]^T, \tag{13}$$

where t^n and t^t denote normal and tangential parts of the traction vector $\mathbf{t}$, respectively. In this work, the tangential component in the interface model is neglected ($t^t=0$), and the normal component has the following form [53]:

$$t^n=g_c^I\frac{w^n}{\left(\delta^n\right)^2}\exp\left(-\frac{w^n}{\delta^n}\right), \tag{14}$$

where δ^n is related to the interface fracture toughness g_c^I and the interface fracture strength t_u by

$$\delta^n=\frac{g_c^I}{t_u\exp\left(1\right)}, \tag{15}$$

w^n is the normal displacement jump defined by $w^n=\mathbf{w}\cdot\mathbf{n}^I$. Two examples of relationship (14) are shown in Fig. 2.

It should be noted that $\beta\left(\mathbf{x}\right)$ and $\mathbf{n}^I$ do not change during the simulation due to the invariable of interfaces. For a sharp interface, the singular part of the strain along the interface can be defined by

$$\boldsymbol{\varepsilon}^I(\mathbf{x})=\mathbf{n}^I(\mathbf{x})\otimes^s[\![\mathbf{u}(\mathbf{x})]\!]\,\delta(\mathbf{x})\quad\forall\mathbf{x}\in\Gamma^I, \tag{16}$$

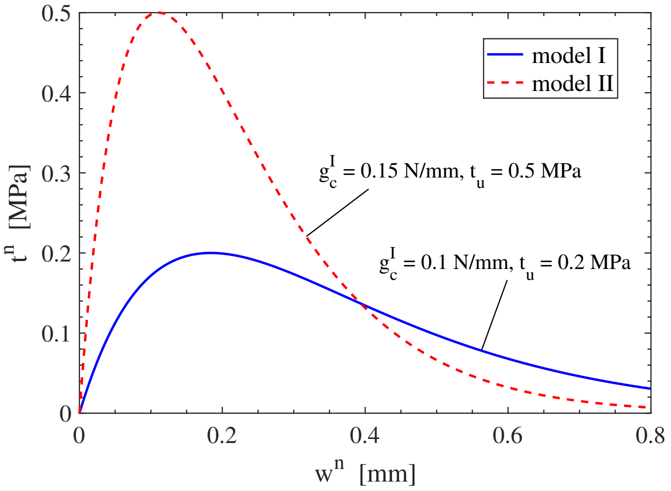

Figure 2: Two cohesive models for analyzing the influences of the interfacial parameters.

then using the above regularized formulation, (16) can be approximated as [50]:

$$\boldsymbol{\varepsilon}^I(\mathbf{x}) \simeq \mathbf{n}^I(\mathbf{x}) \otimes^s \mathbf{w}(\mathbf{x}) \gamma_\beta(\mathbf{x}) \quad \forall \mathbf{x} \in \Omega. \tag{17}$$

It is worth noting that the above three length scale parameters (ℓ_d, ℓ_p and ℓ_β) do not represent physically the exact crack or plastic response width, but the parameters which are used to regularize the discontinuities and plasticity. In the present work, the length scale parameter ℓ_d and ℓ_β are simply chosen according to $\ell_d = \ell_\beta = 2h_e$, where h_e is the minimal element size, h is chosen according to $h = h_e$ to obtain a minimal error for displacement jump (see [50]), $\ell_p \geq \ell_d$ is required such that the regularized crack zone lies inside of the plastic zone as outlined in [30], here $\ell_p = 3h_e$ is used. Interestingly, it has been shown that ℓ_d can be treated as a material parameter associated with the Young's modulus, the tensile strength, and the critical energy release rate of the material in [17, 54, 55]. Possible improvements may imply the use of recent length-free formulations as e.g. proposed in [56], where a length-scale insensitive phase field method for brittle fracture has been proposed.

3. Phase field modeling of elastoplastic dynamic fracture interacting with interfacial damage

In this section, we propose a phase field model for modeling interactions between interfacial debonding and bulk dynamic cracking in elastoplastic composites. The formulation is developed using the variational framework for fracture as introduced in [26].

First, the total strain is defined as:

$$\boldsymbol{\varepsilon} = \boldsymbol{\varepsilon}^e + \boldsymbol{\varepsilon}^p + \boldsymbol{\varepsilon}^I, \tag{18}$$

where $\boldsymbol{\varepsilon}^I$ has been defined in (17) and $\boldsymbol{\varepsilon}^e$ denotes the elastic strain. The plastic incompressibility is assumed, i.e. $\mathrm{Tr}(\boldsymbol{\varepsilon}^p) = 0$, $\mathrm{Tr}(.)$ being the trace operator. In the following, we define the deviatoric parts of the stress and of the elastic strain tensors as $\mathbf{s} = \mathrm{dev}(\boldsymbol{\sigma})$ and $\mathbf{e}^e = \mathrm{dev}(\boldsymbol{\varepsilon}^e)$, respectively, with $\mathrm{dev}(.) = (.) - \frac{1}{3}\mathrm{Tr}(.)\mathbf{1}$, $\mathbf{1}$ being the first-order identity operator.

3.1. Energy functional

Let us consider a two-phase medium which is elasto-plastic and suffers from dynamic loading. Small strains are assumed. The action-integral over a time interval $I = [t_1, t_2]$ in the absence of body forces can be defined as

$$\mathcal{A} = \int_I \left[\int_\Omega \left(\psi^e + \psi^p + \psi^d + \psi^I \right) d\Omega - \int_\Omega \psi^k d\Omega - \int_{\partial\Omega_F} \overline{\mathbf{F}} \cdot \mathbf{u} dS \right] dt, \tag{19}$$

where ψ^e denotes elastic strain energy density, ψ^p denotes the plastic strain energy density, ψ^d is the fracture energy density, ψ^I is a strain density depending on the approximated displacement jump across the interfaces and ψ^k is the kinetic energy density, $\overline{\mathbf{F}}$ is prescribed traction over the boundary $\partial\Omega_F$.

Here, the elastic strain energy density is chosen as

$$\psi^e = g\left(d\right) \psi_0^{e+}\left(\boldsymbol{\varepsilon}^e\right) + \psi_0^{e-}\left(\boldsymbol{\varepsilon}^e\right), \tag{20}$$

with [17]

$$\psi_0^{e+}\left(\boldsymbol{\varepsilon}^e\right) = \frac{1}{2}\kappa \left\langle \mathrm{Tr}\left(\boldsymbol{\varepsilon}^e\right)\right\rangle_+^2 + \mu \mathbf{e}^e : \mathbf{e}^e, \tag{21}$$

$$\psi_0^{e-}\left(\boldsymbol{\varepsilon}^e\right) = \frac{1}{2}\kappa \left\langle \mathrm{Tr}\left(\boldsymbol{\varepsilon}^e\right)\right\rangle_-^2, \tag{22}$$

where, κ and μ denote bulk modulus and shear modulus, respectively, $\langle x \rangle_\pm = \frac{1}{2}\left(x \pm |x|\right)$, $g(d) = (1-d)^2 + k$, k being a small numerical parameter to prevent loss of definite posedness of the elastic tensor for fully broken case.

The plastic strain energy density is here chosen as

$$\psi^p = g\left(d\right) \psi_0^p, \tag{23}$$

where ψ_0^p denotes the initial plastic strain energy density as given in (4). Note that the presence of $g\left(d\right)$ in (23) introduces a strong plasticity-damage coupling into the present model, where the plastic strain energy can also induce the crack initiation and propagation.

The fracture energy density is chosen as

$$\psi^d = \left(1-\beta\right)^2 \psi_0^d, \tag{24}$$

where ψ_0^d denotes the initial fracture energy density. For ψ_0^d, one choice is

$$\psi_0^d = g_c \gamma_d\left(d\right), \tag{25}$$

where γ_d is defined in (3) and g_c denotes the fracture toughness, another choice proposed by Fremond [57] can provide a threshold

$$\psi_0^d = \psi_c \left[2d + \ell_d^2 \nabla d \cdot \nabla d\right]. \tag{26}$$

Note that compared to (25), in (26) d enters the formulation by a linear term. In (26), ψ_c is a specific fracture energy density, which can be further related to a critical fracture stress σ_c by

$$\psi_c = \frac{1}{2E}\sigma_c^2, \tag{27}$$

where E is the Young's modulus. In the present work, the initial fracture energy density in (26) is used in the following.

Following our previous work [50], we give the energy density of interfacial jump component as

$$\psi^I = \overline{\psi}^I(\mathbf{w})\,\gamma_\beta(\beta)\,, \tag{28}$$

where γ_β and $\mathbf{w}$ are defined in (8) and (10), respectively. $\overline{\psi}^I$ is the interface strain density given in (12).

Here, the kinetic energy density has this form

$$\psi^k = \frac{1}{2}\rho\dot{\mathbf{u}}\cdot\dot{\mathbf{u}}, \tag{29}$$

where ρ is the material density and $\dot{\mathbf{u}}$ denotes the velocity.

3.2. Variational formulation

In this section, we use the variational framework for fracture as introduced in [26, 58, 59] to derive the evolution criteria of the proposed model. The variational framework involves: irreversibility condition, stability condition, energy balance and alternate minimization.

3.2.1. Irreversibility condition

The irreversibility condition for fracture and plastic variables is expressed as

$$\dot{d} \geq 0, \quad 0 \leq d \leq 1, \quad \dot{p} \geq 0, \tag{30}$$

the fracture irreversibility condition is prescribed using a history function [18] (see Section 3.2.4), while the plastic irreversibility condition is applied numerically by simply considering the equivalent plastic strain value corresponding to the previous load step as the minimum admissible level of equivalent plastic strain for a given position in the body.

3.2.2. First-order stability condition

We first define the directional derivative as:

$$D_{\mathbf{v}}f(\mathbf{u}) = \left[\frac{d}{dh}f(\mathbf{u}+h\mathbf{v})\right]_{h=0}. \tag{31}$$

The first order stability condition (see [60, 61]) is expressed by

$$D_{\delta\mathbf{u}}\mathcal{A} + D_{\delta p}\mathcal{A} + D_{\delta d}\mathcal{A} \geq 0, \tag{32}$$

which yields by using (19)

$$\int_I\left[\int_\Omega\left(\boldsymbol{\sigma}:\boldsymbol{\varepsilon}^e(\delta\mathbf{u}) + \frac{\partial\psi^I}{\partial\mathbf{w}}\cdot\mathbf{w}(\delta\mathbf{u}) + \rho\ddot{\mathbf{u}}\cdot\delta\mathbf{u}\right)d\Omega - \int_{\partial\Omega_F}\overline{\mathbf{F}}\cdot\delta\mathbf{u}dS\right]dt$$
$$+\int_I\left[\int_\Omega\left(-\sqrt{\frac{3}{2}}\boldsymbol{\sigma}:\hat{\mathbf{n}}\delta p + D_{\delta p}\psi^p\right)d\Omega\right]dt + \int_I\left[\int_\Omega\left(\frac{\partial\psi^e}{\partial d}\delta d + \frac{\partial\psi^p}{\partial d}\delta d + D_{\delta d}\psi^d\right)d\Omega\right]dt \geq 0 \tag{33}$$

where $\hat{\mathbf{n}}$ is a unit tensor in the direction of the plastic flow and the Cauchy stress is given by

$$\boldsymbol{\sigma} = \frac{\partial \psi^e}{\partial \boldsymbol{\varepsilon}^e} = g\left(d\right) \boldsymbol{\sigma}_{\text{eff}}^{+} + \boldsymbol{\sigma}_{\text{eff}}^{-}, \tag{34}$$

where $\boldsymbol{\sigma}_{\text{eff}}^{+}$ and $\boldsymbol{\sigma}_{\text{eff}}^{-}$ are the effective tensile and compressive stresses defined as

$$\boldsymbol{\sigma}_{\text{eff}}^{+} = \frac{\partial \psi_0^{e+}}{\partial \boldsymbol{\varepsilon}^e} = \kappa \left\langle \text{Tr}\left(\boldsymbol{\varepsilon}^e\right)\right\rangle_+ \mathbf{1} + 2\mu \mathbf{e}^e, \quad \boldsymbol{\sigma}_{\text{eff}}^{-} = \frac{\partial \psi_0^{e-}}{\partial \boldsymbol{\varepsilon}^e} = \kappa \left\langle \text{Tr}\left(\boldsymbol{\varepsilon}^e\right)\right\rangle_- \mathbf{1}. \tag{35}$$

From (33), the following results stem out:

- For $\delta p = \delta d = 0$, the time interval $I = [t_1, t_2]$ is arbitrary the integrand must sum to zero so that finally

$$\int_\Omega \boldsymbol{\sigma} : \boldsymbol{\varepsilon}^e\left(\delta \mathbf{u}\right) d\Omega + \int_\Omega \gamma_\beta \mathbf{t} \cdot \mathbf{w}\left(\delta \mathbf{u}\right) d\Omega + \int_\Omega \rho \ddot{\mathbf{u}} \cdot \delta \mathbf{u} d\Omega - \int_{\partial \Omega_F} \overline{\mathbf{F}} \cdot \delta \mathbf{u} dS = 0 \tag{36}$$

  which is the weak form of the equilibrium equation.

- For $\delta d = 0$ and $\delta \mathbf{u} = \mathbf{0}$, we first express the term:

$$D_{\delta p} \psi^p = g\left(d\right)\left(\sigma_y \delta p + H p \delta p + \sigma_0 \ell_p^2 \nabla p \cdot \nabla \delta p\right), \tag{37}$$

  considering that the time interval $I = [t_1, t_2]$ is arbitrary, (33) yields:

$$\int_\Omega \left[\left(\sqrt{\frac{3}{2}} \left\|\mathbf{s}\right\| - g\left(d\right)\left(\sigma_y + H p\right)\right) \delta p - g\left(d\right) \sigma_0 \ell_p^2 \nabla p \cdot \nabla \delta p\right] d\Omega \leq 0, \tag{38}$$

  which is the weak form of the plasticity yield criterion. The local form of the plastic yield criterion can be expressed as

$$\mathcal{F}^p = \sqrt{\frac{3}{2}} \left\|\mathbf{s}\right\| - g\left(d\right)\left(\sigma_y + H p - \sigma_0 \ell_p^2 \nabla \cdot \nabla p\right) \leq 0 \quad \text{in} \quad \Omega. \tag{39}$$

- Similarily for $\delta p = 0$ and $\delta \mathbf{u} = \mathbf{0}$, (33) yields:

$$\begin{aligned} \int_\Omega \Bigg\{ & \left(1 - d\right)\left[\psi_0^{e+} + \sigma_y p + \frac{1}{2} H p^2 + \frac{1}{2} \sigma_0 \ell_p^2 \nabla p \cdot \nabla p - \left(1 - \beta\right)^2 \psi_c\right] \delta d \\ & - \left(1 - \beta\right)^2 \left(\psi_c d \delta d + \psi_c \ell_d^2 \nabla d \cdot \nabla \delta d\right) \Bigg\} d\Omega \leq 0, \end{aligned} \tag{40}$$

  which is the weak form of the damage yield criterion. The local form of the damage yield criterion can be expressed as

$$\begin{aligned} \mathcal{F}^d = & \left(1 - d\right)\left[\psi_0^{e+} + \sigma_y p + \frac{1}{2} H p^2 + \frac{1}{2} \sigma_0 \ell_p^2 \nabla p \cdot \nabla p - \left(1 - \beta\right)^2 \psi_c\right] \\ & - \left(1 - \beta\right)^2 \left(\psi_c d - \psi_c \ell_d^2 \nabla \cdot \nabla d\right) \leq 0 \quad \text{in} \quad \Omega. \end{aligned} \tag{41}$$

3.2.3. Energy balance

Following a procedure analogous to the treatment of the stability condition, the energy balance condition leads to

$$\int_I \left[-\int_\Omega \left(\boldsymbol{\sigma} : \boldsymbol{\varepsilon}^e(\dot{\mathbf{u}}) + \frac{\partial \psi^I}{\partial \mathbf{w}} \cdot \mathbf{w}(\dot{\mathbf{u}}) + \rho \ddot{\mathbf{u}} \cdot \dot{\mathbf{u}} \right) d\Omega + \int_{\partial\Omega_F} \overline{\mathbf{F}} \cdot \dot{\mathbf{u}} dS \right] dt$$

$$+ \int_I \left[\int_\Omega \left(\sqrt{\frac{3}{2}} \boldsymbol{\sigma} : \hat{\mathbf{n}} \dot{p} - D_{\dot{p}} \psi^p \right) d\Omega \right] dt - \int_I \left[\int_\Omega \left(\frac{\partial \psi^e}{\partial d} \dot{d} + \frac{\partial \psi^p}{\partial d} \dot{d} + D_{\dot{d}} \psi^d \right) d\Omega \right] dt = 0 \tag{42}$$

Considering that the time interval $I = [t_1, t_2]$ is arbitrary, the following cases are analyzed:

- For $\dot{\mathbf{u}} = \mathbf{0}$ and $\dot{d} = 0$, the plasticity consistency condition is obtained:

$$\mathcal{F}^p \dot{p} = 0 \tag{43}$$

- For $\dot{\mathbf{u}} = \mathbf{0}$ and $\dot{p} = 0$, the damage consistency condition can be written in the form:

$$\mathcal{F}^d \dot{d} = 0 \tag{44}$$

where $\mathcal{F}^p$ and $\mathcal{F}^d$ are given in (39) and (41), respectively.

3.2.4. Alternate minimization

In this section, a staggered alternate minimization algorithm for $\mathbf{u}$, p and d is applied. With the total energy (19) at hand, the alternate minimization follows.

- Minimizing with respect to the displacement field:

$$D_{\delta\mathbf{u}} \mathcal{A} = \int_I \left[\int_\Omega \boldsymbol{\sigma} : \boldsymbol{\varepsilon}^e(\delta\mathbf{u}) d\Omega + \int_\Omega \gamma_\beta \mathbf{t} \cdot \mathbf{w}(\delta\mathbf{u}) d\Omega + \int_\Omega \rho \ddot{\mathbf{u}} \cdot \delta\mathbf{u} d\Omega - \int_{\partial\Omega_F} \overline{\mathbf{F}} \cdot \delta\mathbf{u} dS \right] dt = 0 \tag{45}$$

  which fits arbitrary $I = [t_1, t_2]$ and thus leads to

$$R_{\mathbf{u}} = \int_\Omega \boldsymbol{\sigma} : \boldsymbol{\varepsilon}^e(\delta\mathbf{u}) d\Omega + \int_\Omega \gamma_\beta \mathbf{t} \cdot \mathbf{w}(\delta\mathbf{u}) d\Omega + \int_\Omega \rho \ddot{\mathbf{u}} \cdot \delta\mathbf{u} d\Omega - \int_{\partial\Omega_F} \overline{\mathbf{F}} \cdot \delta\mathbf{u} dS = 0 \tag{46}$$

  which is the weak form of the mechanical problem to be solved for $\mathbf{u}$, given p and d.

- Minimizing with respect to the equivalent plastic strain, we can then obtain:

$$R_p = \int_\Omega \left\{ \left[\sqrt{\frac{3}{2}} \|\mathbf{s}\| - g(d)(\sigma_y + Hp) \right] \delta p - g(d) \sigma_0 \ell_p^2 \nabla p \cdot \nabla \delta p \right\} d\Omega = 0, \tag{47}$$

  which is the weak form of the plastic yield criterion to be solved for p with $\dot{p} \geq 0$, given $\mathbf{u}$ and d. The increment of the plastic strain tensor can be obtained from the incremental equivalent plastic strain as

$$\dot{\boldsymbol{\varepsilon}}^p = \sqrt{\frac{3}{2}} \dot{p} \frac{\mathbf{s}}{\|\mathbf{s}\|} \tag{48}$$

- Minimizing with respect to the damage field, we can then obtain:

$$\begin{aligned} R_d = \int_\Omega \Bigg\{ & (1-d)\left[\psi_0^{e+} + \sigma_y p + \frac{1}{2}Hp^2 + \frac{1}{2}\sigma_0 \ell_p^2 \nabla p \cdot \nabla p - (1-\beta)^2 \psi_c\right]\delta d \\ & - (1-\beta)^2 \left(\psi_c d\delta d + \psi_c \ell_d^2 \nabla d \cdot \nabla \delta d\right) \Bigg\} d\Omega = 0. \end{aligned} \tag{49}$$

To prescribe damage irreversibility, a history function inspired by [18] is given as

$$\mathcal{H} = \max_{s\in[0,t]} \left[\left\langle \psi_0^{e+}(\boldsymbol{\varepsilon}^e, s) + \sigma_y p(s) + \frac{1}{2}Hp(s)^2 + \frac{1}{2}\sigma_0 \ell_p^2 \nabla p(s) \cdot \nabla p(s) - (1-\beta)^2 \psi_c \right\rangle_+\right], \tag{50}$$

then we can rewrite (49) as

$$R_d = \int_\Omega \left[(1-d)\,\mathcal{H}\delta d - (1-\beta)^2 \left(\psi_c d\delta d + \psi_c \ell_d^2 \nabla d \cdot \nabla \delta d\right)\right] d\Omega = 0, \tag{51}$$

which corresponds to the global damage problem to be solved to find the field $d(\mathbf{x})$, given $\mathbf{u}$ and p.

4. Discretization and numerical implementation

In this section, we detail the finite element discretizations for displacement, plastic and damage problems, and finally provide the overall algorithm. It should be noticed that, in this paper, due to the regularization of plasticity, the plastic problem is handled through solving a global problem for equivalent plastic strain p as shown in [58], unlike our previous work [62], where the plastic problem is treated as a local one (at Gauss integration points) and solved by using the return-mapping algorithm.

4.1. Displacement problem

In this work, for the sake of clarity, only 2D FEM discretization is detailed. The vector form of second-order tensors are introduced as $[\boldsymbol{\varepsilon}] = \left[\varepsilon_{11},\ \varepsilon_{22},\ \sqrt{2}\varepsilon_{12}\right]^T$, $[\boldsymbol{\sigma}] = \left[\sigma_{11},\ \sigma_{22},\ \sqrt{2}\sigma_{12}\right]^T$, as well as the FEM approximations

$$\mathbf{u} = \mathbf{N_u}\mathbf{u}^e, \quad [\boldsymbol{\varepsilon}] = \mathbf{B_u}\mathbf{u}^e, \quad \mathbf{w} = h\mathbf{N}\mathbf{B}\mathbf{u}^e, \quad [\boldsymbol{\varepsilon}^e + \boldsymbol{\varepsilon}^p] = \mathbf{B_w}\mathbf{u}^e, \tag{52}$$

where $\mathbf{u}^e$ denotes nodal displacement components in one element, $\mathbf{N_u}$ is a matrix of displacement shape function, $\mathbf{B_u}$ is a matrix of displacement shape function derivatives, and

$$\mathbf{N} = \begin{bmatrix} n_1 & n_2 & 0 & 0 \\ 0 & 0 & n_1 & n_2 \end{bmatrix}, \quad \mathbf{B} = \begin{bmatrix} \frac{\partial}{\partial x_1} & \frac{\partial}{\partial x_2} & 0 & 0 \\ 0 & 0 & \frac{\partial}{\partial x_1} & \frac{\partial}{\partial x_2} \end{bmatrix}^T \mathbf{N_u}, \tag{53}$$

where n_1 and n_2 are the x- and y- components of the normal vector $\mathbf{n}^I$ in (11), $\mathbf{B_w}$ is a modified spatial strain-displacement matrix defined by

$$\mathbf{B_w} = \mathbf{B_u} - h\gamma_\beta \mathbf{Q}\mathbf{B} \tag{54}$$

in which $\mathbf{Q}$ is a matrix expressed by

$$\mathbf{Q}=\begin{bmatrix} n_1 & 0 \\ 0 & n_2 \\ \frac{1}{\sqrt{2}}n_2 & \frac{1}{\sqrt{2}}n_1 \end{bmatrix} \mathbf{N}=\begin{bmatrix} n_1^2 & n_1n_2 & 0 & 0 \\ 0 & 0 & n_1n_2 & n_2^2 \\ \frac{1}{\sqrt{2}}n_1n_2 & \frac{1}{\sqrt{2}}n_2^2 & \frac{1}{\sqrt{2}}n_1^2 & \frac{1}{\sqrt{2}}n_1n_2 \end{bmatrix}. \tag{55}$$

After rearranging, the discrete version of (46) can be expressed globally as

$$\mathbf{M}\ddot{\mathbf{u}}+\mathbf{K}_u\mathbf{u}=\mathbf{F}_u \tag{56}$$

with

$$\mathbf{M}=\int_\Omega \rho\mathbf{N}_\mathbf{u}^T\mathbf{N}_\mathbf{u}d\Omega, \qquad \mathbf{K}_u=\int_\Omega \mathbf{B}_\mathbf{w}^T\mathbf{C}\mathbf{B}_\mathbf{w}d\Omega \tag{57}$$

$$\mathbf{F}_u=\int_\Omega \mathbf{B}_\mathbf{w}^T\mathbf{C}\boldsymbol{\varepsilon}^{p,(k)}d\Omega+\int_{\partial\Omega_F}\mathbf{N}_\mathbf{u}^T\overline{\mathbf{F}}dS-\int_\Omega \gamma_\beta\left(h\mathbf{N}\mathbf{B}\right)^T\mathbf{t}\left(\mathbf{w}^{(k)}\right)d\Omega \tag{58}$$

where

$$\mathbf{C}=\begin{cases} g\left(d\right)\left(\kappa\mathbf{II}+2\mu\mathbf{II}_d\right) & \mathrm{Tr}\left(\boldsymbol{\varepsilon}^e\right)\geq 0 \\ \kappa\mathbf{II}+g\left(d\right)2\mu\mathbf{II}_d & \mathrm{Tr}\left(\boldsymbol{\varepsilon}^e\right)<0 \end{cases} \tag{59}$$

$$\mathbf{II}=\begin{bmatrix} 1 & 1 & 0 \\ 1 & 1 & 0 \\ 0 & 0 & 0 \end{bmatrix}, \quad \mathbf{II}_d=\begin{bmatrix} \frac{1}{2} & -\frac{1}{2} & 0 \\ -\frac{1}{2} & \frac{1}{2} & 0 \\ 0 & 0 & 1 \end{bmatrix}. \tag{60}$$

Above, $(.)^{(k)}$ denotes the value of k-th subiteration for each time step.

Then, an unconditionally stable implicit Newmark scheme is employed to solve (56) according to

$$\dot{\mathbf{u}}^n=\dot{\mathbf{u}}^{n-1}+\frac{\Delta t}{2}\left(\ddot{\mathbf{u}}^{n-1}+\ddot{\mathbf{u}}^n\right) \tag{61}$$

with

$$\mathbf{u}^n=\mathbf{u}^{n-1}+\Delta t\dot{\mathbf{u}}^{n-1}+\left(\frac{\Delta t}{2}\right)^2\left(\ddot{\mathbf{u}}^{n-1}+\ddot{\mathbf{u}}^n\right) \tag{62}$$

$$\ddot{\mathbf{u}}^n=\left(\frac{2}{\Delta t}\right)^2\left(\mathbf{u}^n-\hat{\mathbf{u}}^n\right) \tag{63}$$

$$\hat{\mathbf{u}}^n=\mathbf{u}^{n-1}+\Delta t\dot{\mathbf{u}}^{n-1}+\left(\frac{\Delta t}{2}\right)^2\ddot{\mathbf{u}}^{n-1}, \tag{64}$$

where $(.)^n$ denotes the value of n-th time step and $\Delta t=t^n-t^{n-1}$ is assumed to be constant.

Introducing (63) into (56), the linear problem to be solved for displacement at subiteration k of one time step t^n can be obtained as

$$\tilde{\mathbf{K}}_u^n \mathbf{u}^n = \tilde{\mathbf{F}}_u^n \tag{65}$$

with

$$\tilde{\mathbf{K}}_u^n = \left(\frac{2}{\Delta t}\right)^2 \mathbf{M} + \mathbf{K}_u^n \tag{66}$$

$$\tilde{\mathbf{F}}_u^n = \mathbf{F}_u^n + \mathbf{M}\left(\frac{2}{\Delta t}\right)^2 \left[\mathbf{u}^{n-1} + \Delta t \dot{\mathbf{u}}^{n-1} + \left(\frac{\Delta t}{2}\right)^2 \ddot{\mathbf{u}}^{n-1}\right] \tag{67}$$

4.2. Plastic problem

We first rewrite (48) with small pseudo-time step assumption as

$$\Delta\varepsilon^p = \sqrt{\frac{3}{2}} \Delta p \frac{\mathbf{s}}{\|\mathbf{s}\|} \tag{68}$$

where $\Delta p = p^n - p^{n-1}$ is the incremental equivalent plastic strain. Then we can rewrite (47) as

$$R_p = \int_\Omega g(d) \left[\left(\sqrt{\frac{3}{2}} \left\|\mathbf{s}_{\text{eff}}^{\text{tr}}\right\| - 3\mu p + 3\mu p^{n-1} - \sigma_y - Hp \right) \delta p - \sigma_0 \ell_p^2 \nabla p \cdot \nabla \delta p \right] d\Omega = 0, \tag{69}$$

where $\mathbf{s}_{\text{eff}}^{\text{tr}}$ denotes a non-plastic trial stress. Here, for the sake of simplicity, the superscript n for p^n is omitted. Notice that Eq.(69) is based on an explicit Euler algorithm and thus require a small time step to ensure accuracy and convergence.

The equivalent plastic strain and equivalent plastic strain gradient are approximated in one element by

$$p = \mathbf{N}_p \mathbf{p}^e, \qquad \nabla p = \mathbf{B}_p \mathbf{p}^e, \tag{70}$$

where $\mathbf{N}_p$ and $\mathbf{B}_p$ are matrices of equivalent plastic strain shape function and of equivalent plastic strain shape function derivatives, respectively, and $\mathbf{p}^e$ denotes nodal equivalent plastic strain in one element.

The discretization of plastic problem (69) results into the following discrete system of equations

$$\mathbf{K}_p \mathbf{p} = \mathbf{F}_p \tag{71}$$

with

$$\mathbf{K}_p = \int_\Omega g(d) \left[(3\mu + H) \mathbf{N}_p^T \mathbf{N}_p + \sigma_0 \ell_p^2 \mathbf{B}_p^T \mathbf{B}_p \right] d\Omega \tag{72}$$

$$\mathbf{F}_p = \int_\Omega g(d) \mathbf{N}_p^T \left(\sqrt{\frac{3}{2}} \left\|\mathbf{s}_{\text{eff}}^{\text{tr}}\right\| + 3\mu p^{n-1} - \sigma_y \right) d\Omega. \tag{73}$$

It is noted that the present work solves the gradient plasticity as a global problem by finite-element method, naturally avoiding unphysical oscillations at the elastic-plastic boundary (reported in [31]) inducing by directly using the return-mapping algorithm in finite-element implementations.

4.3. Damage problem

The damage and damage gradient are approximated in one element by

$$d = \mathbf{N}_d \mathbf{d}^e, \qquad \nabla d = \mathbf{B}_d \mathbf{d}^e, \tag{74}$$

where $\mathbf{N}_d$ and $\mathbf{B}_d$ denote matrices of damage shape function and of damage shape function derivatives, respectively, and $\mathbf{d}^e$ denotes nodal damage in one element.

The discretization of damage problem (51) results into the following discrete system of equations

$$\mathbf{K}_d \mathbf{d} = \mathbf{F}_d \tag{75}$$

with

$$\mathbf{K}_d = \int_\Omega \left\{ \left[\mathcal{H} + (1-\beta)^2 \psi_c \right] \mathbf{N}_d^T \mathbf{N}_d + (1-\beta)^2 \psi_c \ell_d^2 \mathbf{B}_d^T \mathbf{B}_d \right\} d\Omega \tag{76}$$

$$\mathbf{F}_d = \int_\Omega \mathbf{N}_d^T \mathcal{H} \; d\Omega, \tag{77}$$

where $\mathcal{H}$ is given in (50).

4.4. Overall algorithm

In the present work, a staggered iterative scheme is employed following [58]. It consists of solving successively (65), (71) and (75). First, (65) is solved to obtain $\mathbf{u}^{n,(k+1)}$ with given $\left(\mathbf{u}^{n,(k)}, p^{n,(k)}, d^{n,(k)}\right)$, n and k denoting the time step and subiteration, respectively. In a second step, (71) is solved to obtain $p^{n,(k+1)}$ with given $\left(\mathbf{u}^{n,(k+1)}, p^{n,(k)}, d^{n,(k)}\right)$. In a third step, (75) is solved to obtain $d^{n,(k+1)}$ with given $\left(\mathbf{u}^{n,(k+1)}, p^{n,(k+1)}, d^{n,(k)}\right)$. At each time step, the subiteration is performed until convergence is achieved by using three independent tolerances t_u, t_p and t_d. The detailed algorithm is illustrated in Algorithm 1.

Algorithm 1: Overall algorithm

```
Initialize $\mathbf{u}^0$, $p^0$ and $d^0$ with assumption of elasticity and undamaged state;
for $n = 1, \dots, m$ (Loop over all time steps) do
    $k = 0$,  $erru = errp = errd = 1$
    $\mathbf{u}^{n,(0)} = \mathbf{u}^{n-1}$,  $p^{n,(0)} = p^{n-1}$,  $d^{n,(0)} = d^{n-1}$
    while $erru > t_u$ or $errp > t_p$ or $errd > t_d$ and $k \leq k_{max}$ do
        Given $\mathbf{u}^{n,(k)}$, $p^{n,(k)}$ and $d^{n,(k)}$, compute $\mathbf{u}^{n,(k+1)}$ from (65)
        Given $\mathbf{u}^{n,(k+1)}$, $p^{n,(k)}$ and $d^{n,(k)}$, compute $p^{n,(k+1)}$ from (71)
        Given $\mathbf{u}^{n,(k+1)}$, $p^{n,(k+1)}$ and $d^{n,(k)}$, compute $d^{n,(k+1)}$ from (75)
        $erru = \left\| \mathbf{u}^{n,(k+1)} - \mathbf{u}^{n,(k)} \right\|$,  $errp = \left\| p^{n,(k+1)} - p^{n,(k)} \right\|$,  $errd = \left\| d^{n,(k+1)} - d^{n,(k)} \right\|$
        $k = k + 1$
    end
    $\mathbf{u}^n = \mathbf{u}^{n,(k+1)}$,  $p^n = p^{n,(k+1)}$,  $d^n = d^{n,(k+1)}$
end
```

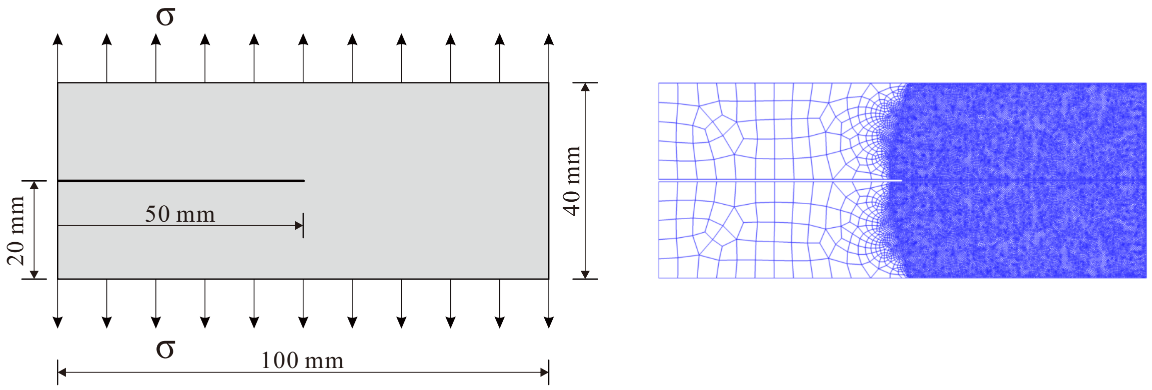

Figure 3: Dynamic crack branching: geometry of the edge cracked block (left) and random finite element mesh with a refined zone ($h_e = 0.25$ mm) in the expected propagation zone (right).

5. Numerical examples

In this section, all numerical computations are performed within the finite element framework. For the sake of clarity, we recall that the length scale parameter ℓ_d and ℓ_β are simply chosen according to $\ell_d = \ell_\beta = 2h_e$, where h_e is the minimal element size, h is chosen according to $h = h_e$ to obtain a minimal error for displacement jump, $\ell_p \geq \ell_d$ is required such that the regularized crack zone lies inside of the plastic zone, here $\ell_p = 3h_e$ is used.

5.1. Dynamic crack branching

In this example, we consider a notched block loaded dynamically in tension. As shown in Fig. 3, a tensile load of $\sigma = 1.0$ MPa is applied at the top and bottom edges of the specimen and held constant throughout the course of the simulation. This problem has been widely adopted to study dynamic crack branching in previous works, including [19] and [44], to name a few.

The material parameters used in the simulations are taken from [44]: Young's modulus 32000 MPa, Poisson's ratio of 0.2, the mass density of $\rho = 2450$ kg/m^3, the yield stress $\sigma_y = 2$ MPa, hardening modulus $H = 0$ MPa.

5.1.1. 2D model with plain strain assumption

In order to verify our implementation, we compare our fracture pattern to ones obtained in [44]. For this purpose, we do not set interface ($\beta = 0$) in the specimen as shown in Fig. 3. The spatial discretization comprises 36196 4-node quadrilateral elements, with refinement in the right region (the minimal element size $h_e = 0.25$ mm) where the crack is expected to propagate (see Fig. 3). The time step is set to $\Delta t = 0.1$ μs. Plain strain conditions are assumed.

The final fracture patterns obtained from different σ_c as well as reference result in [44] are shown in Fig. 4. We illustrate that the fracture patterns obtained by this proposed model have a good agreement with the reference result especially for $\sigma_c = 10$ MPa. Thus, $\sigma_c = 10$ MPa is used in the following unless otherwise stated. The effect of the critical fracture stress σ_c on fracture energy and plastic energy is shown in Fig. 5. As can be observed, with the decrease of the critical fracture stress σ_c, both the fracture initiation time and the final failure time decrease, the maximum fracture energy and plastic energy tend to decrease, besides the width of the fracture zone shows a decreasing trend.

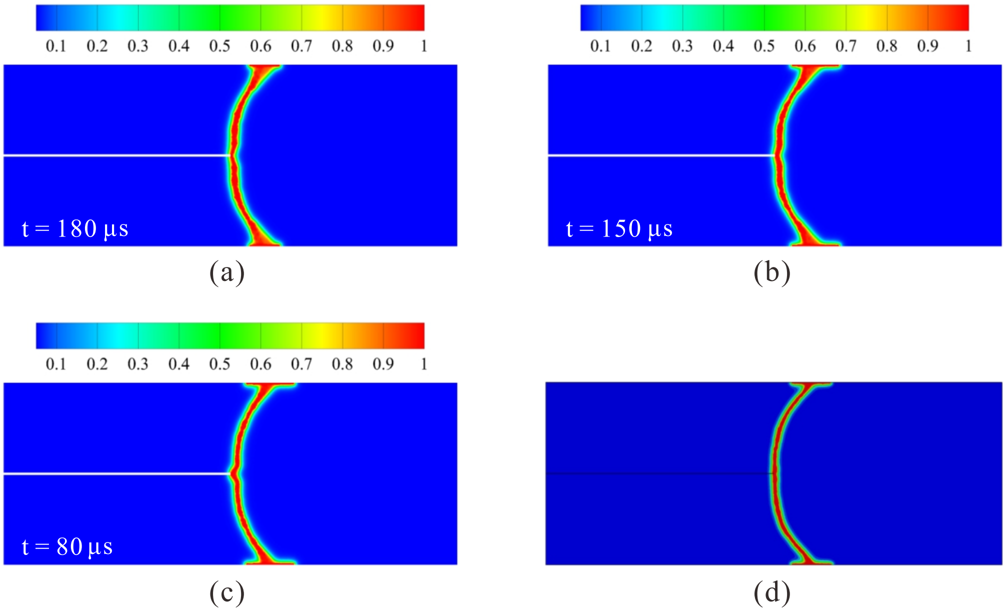

(a) (b) (c) (d)

Figure 4: 2D dynamic crack branching: final fracture patterns for (a) $\sigma_c = 20$ MPa, (b) $\sigma_c = 15$ MPa, (c) $\sigma_c = 10$ MPa and (d) reference [44].

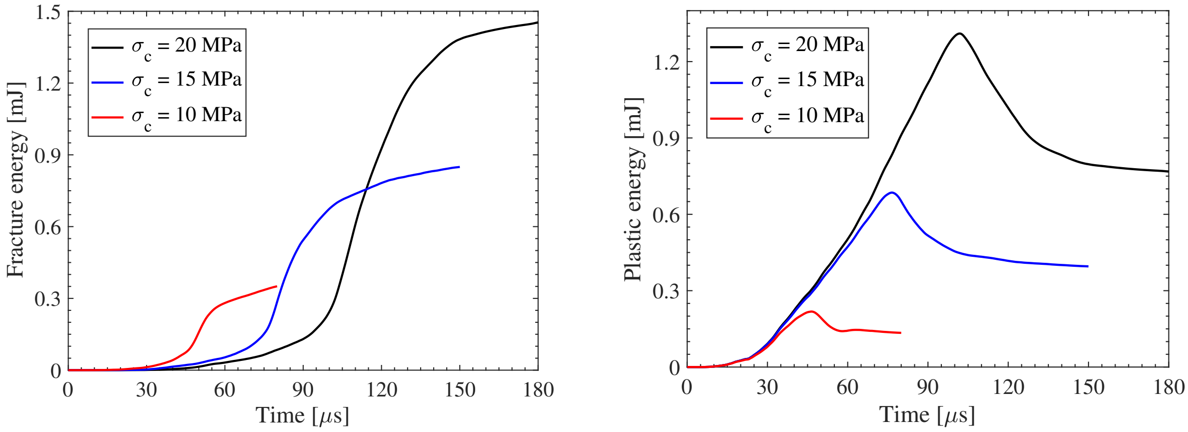

Figure 5: 2D dynamic crack branching: effect of the critical fracture stress σ_c on fracture energy (left) and plastic energy (right).

Further, we analyze the influence of the time increment Δt in the numerical simulation. For this purpose, another two simulations are performed with $\Delta t = 0.05$ μs and $\Delta t = 0.2$ μs, respectively. The corresponding fracture patterns and fracture/plastic energy curves are presented in Fig. 6 and Fig. 7, respectively. The results confirm the stability of the easy-to-implement staggered algorithm as soon as sufficiently small time steps are used. We notice that $\Delta t = 0.1$ μs is small enough for the numerical simulations, thus $\Delta t = 0.1$ μs is used in the following unless otherwise stated.

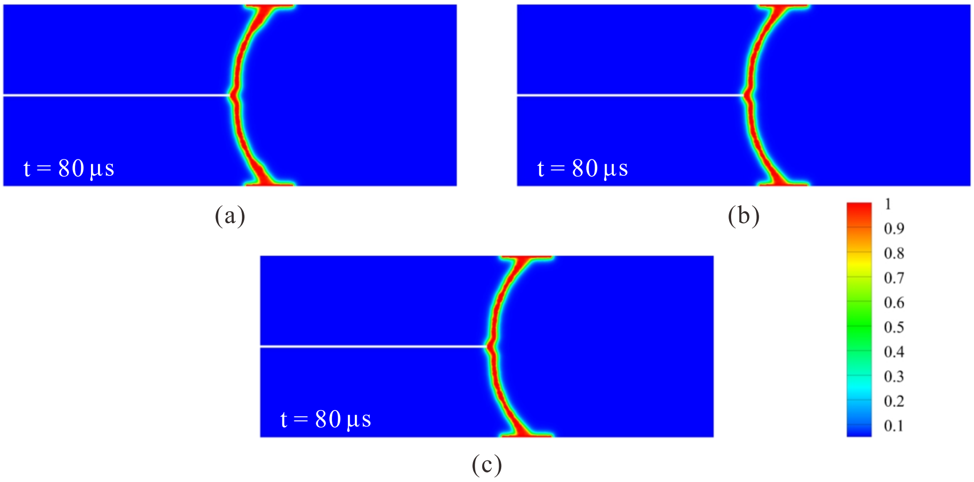

(a)

(b)

(c)

Figure 6: 2D dynamic crack branching: final fracture patterns for (a) $\Delta t = 0.2$ μs, (b) $\Delta t = 0.1$ μs and (c) $\Delta t = 0.05$ μs.

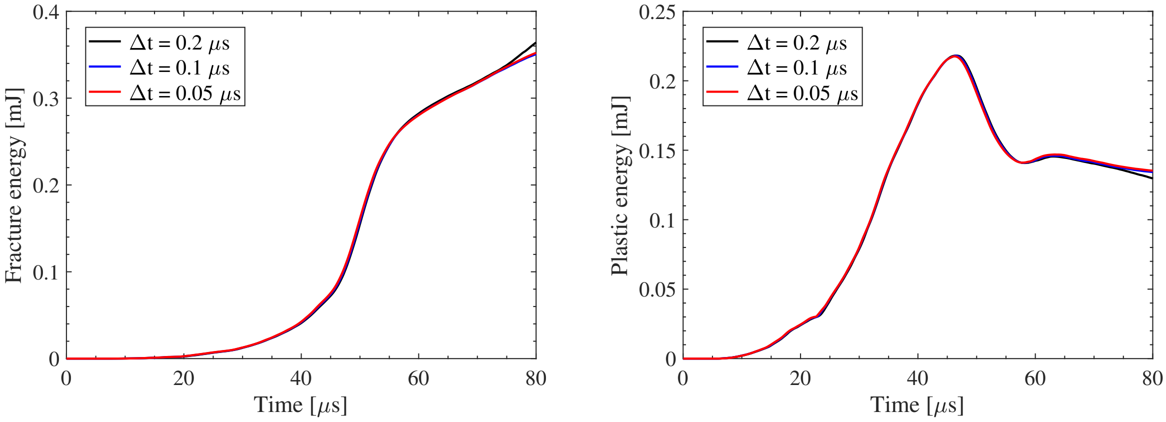

Figure 7: 2D dynamic crack branching. Convergence of the solution with respect to the time increments in the numerical simulation: fracture energy (left) and plastic energy (right).

5.1.2. 3D model

To eliminate the influence of plain strain assumption used in 2D model and better investigate the performance of the proposed model, a 3D model with the same geometry as shown in Fig. 3 whereas thickness 0.25 mm in the z direction is investigated. The spatial discretization of the 3D model comprises 237734 tetrahedral elements, with refinement in the right region ($h_e = 0.25$ mm) as shown in Fig. 8d.

Then we continue to investigate the dynamic crack branching by employing the above 3D model and the same parameters used in the 2D model, notice the interface is still not considered. Fig. 8a shows the final fracture pattern, as can be seen, the fracture pattern exhibits an obvious difference with the 2D fracture patterns shown in Fig. 4. This phenomenon can also be found in the reference [44]. Next we investigate the effect of the yield stress σ_y on the final crack patterns and fracture/plastic energy. The corresponding results are shown in Fig. 8 and Fig. 9, respectively.

It can be seen that, as the yield stress is increased, the final crack pattern trends to become the result obtained by quasi-brittle dynamic fracture model. In order to better consider plasticity, we continue to use $\sigma_y = 2$ MPa in the following unless otherwise stated.

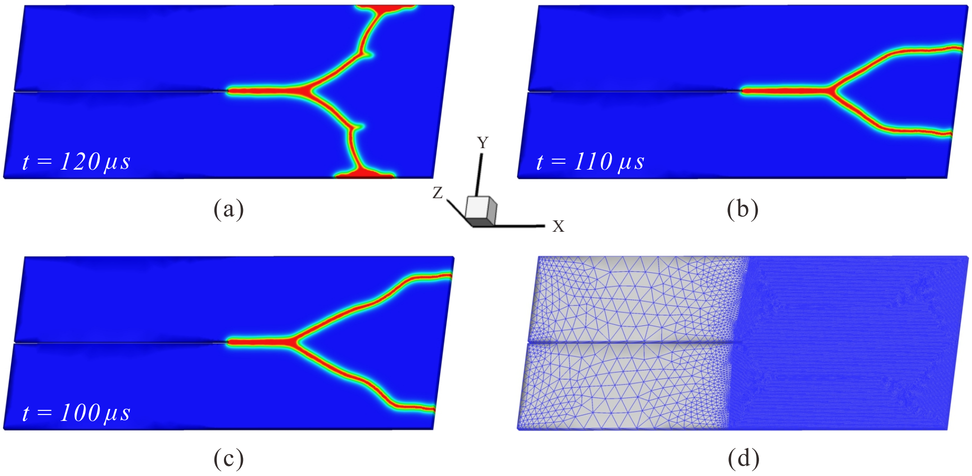

Figure 8: 3D dynamic crack branching: final fracture patterns for (a) $\sigma_y = 2$ MPa, (b) $\sigma_y = 3$ MPa and (c) $\sigma_y = 4$ MPa; (d) 3D mesh model with a refined zone ($h_e = 0.25$ mm).

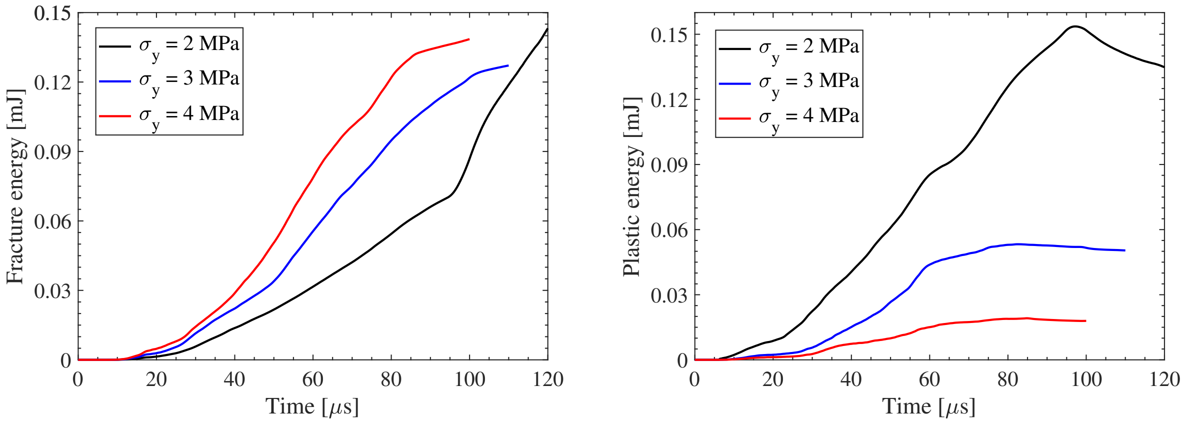

Figure 9: 3D dynamic crack branching: effect of the yield stress σ_y on fracture energy (left) and plastic energy (right).

Further, we investigate the influence of the interface by setting an interface in the 3D model as shown in Fig. 10a. For this purpose, two sets of parameters for the cohesive model (defined in (14)), as illustrated in Fig. 2, are considered to illustrate the effect of the interfacial effect on crack patterns and fracture/plastic energy. The mesh model shown in Fig. 8d is used in the numerical simulations. The corresponding results are shown in Fig. 10 and Fig. 11, respectively. We can observe that, compared to no interface, the presence of the interface has an obvious influence on the crack patterns and fracture/plastic energy, and when considering interfacial damage and changing the cohesive parameters, both the fracture patterns and fracture/plastic energy are very similar.

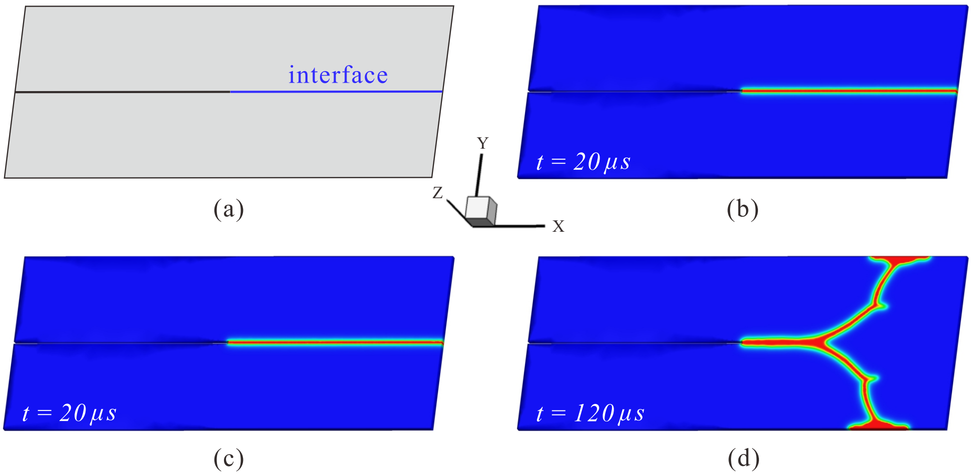

Figure 10: 3D model with interface: (a) 3D model, (b) fracture pattern obtained by model I, (c) fracture pattern obtained by model II and (d) fracture pattern without considering interface.

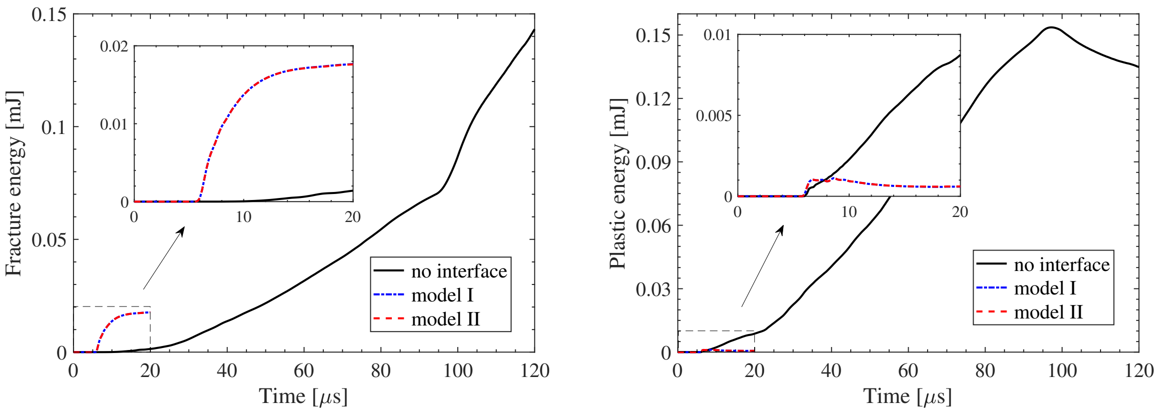

Figure 11: 3D model with interface: effect of the different interfacial damage model on fracture energy (left) and plastic energy (right).

Then, we test the convergence of the model with respect to the mesh refinement. For this purpose, the previous simulation used the parameters in model I is conducted with another two refined meshes with 362976 elements and 498246 elements, respectively. Fig. 12 shows the final fracture patterns for the three mesh models. Fig. 13 shows the fracture/plastic energy for the three mesh models. The results show the convergence of the method with mesh refinement.

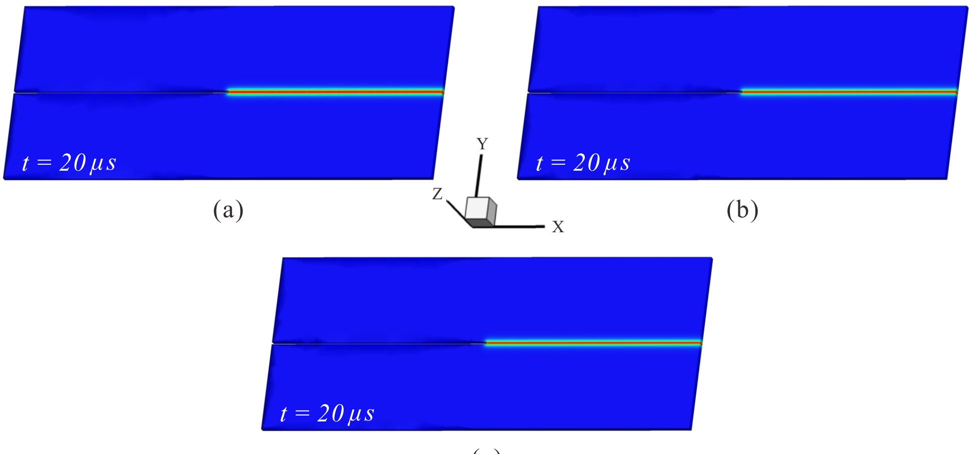

(a) (b) (c)

Figure 12: 3D model with interface. The final fracture patterns for (a) mesh 1 (237734 elements), (b) mesh 2 (362976 elements) and (c) mesh 3 (498246 elements).

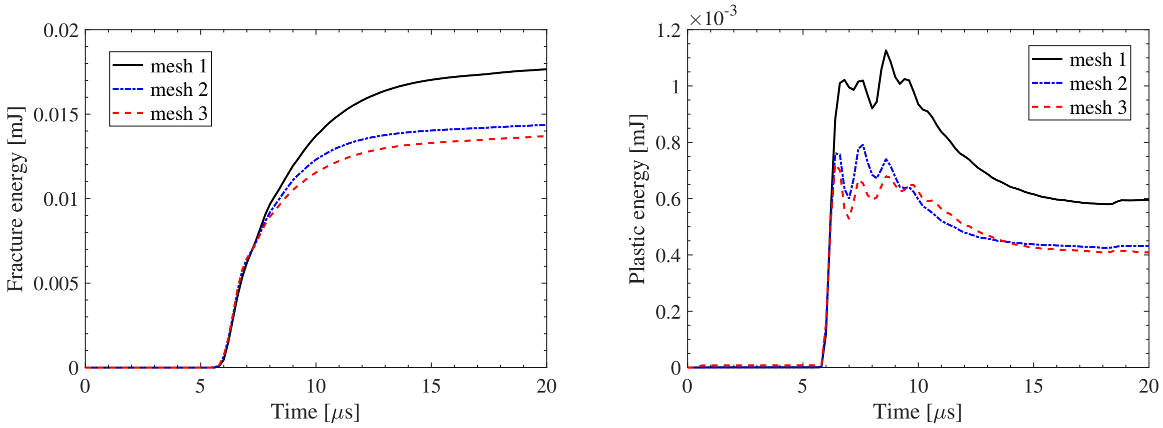

Figure 13: 3D model with interface. The fracture energy (left) and plastic energy (right) for mesh 1 (237734 elements), mesh 2 (362976 elements) and mesh 3 (498246 elements).

5.2. 3D rectangular plate with cylindrical fibers

In this example, we investigate the proposed model through a complex structure which has several cylindrical fibers, as shown in Fig. 14. The dimensions of the 3D structure in x-y plane are 80×40 mm^2, and in order to ensure the used element number within an appropriate range, the thickness of the 3D structure is chosen as 0.25 mm. As can be observed from Fig. 14, there are five cylindrical fibers named by "F1-F5 ", whose diameters are 20 mm (F1), 10 mm (F2-F4) and 8 mm (F5), respectively. The coordinates of the central axis for the five cylindrical fibers in the basis (x, y) are $(20, 20)$, $(45, 20)$, $(60, 30)$, $(60, 10)$ and $(70, 20)$, respectively. Similarly, a tensile load of $\sigma = 2.0$ MPa is applied at the top and bottom edges of the specimen and held constant throughout the course of the simulation. The spatial discretization of the 3D model comprises 356938 tetrahedral elements with the minimal element size $h_e = 0.25$ mm, as shown in Fig. 14.

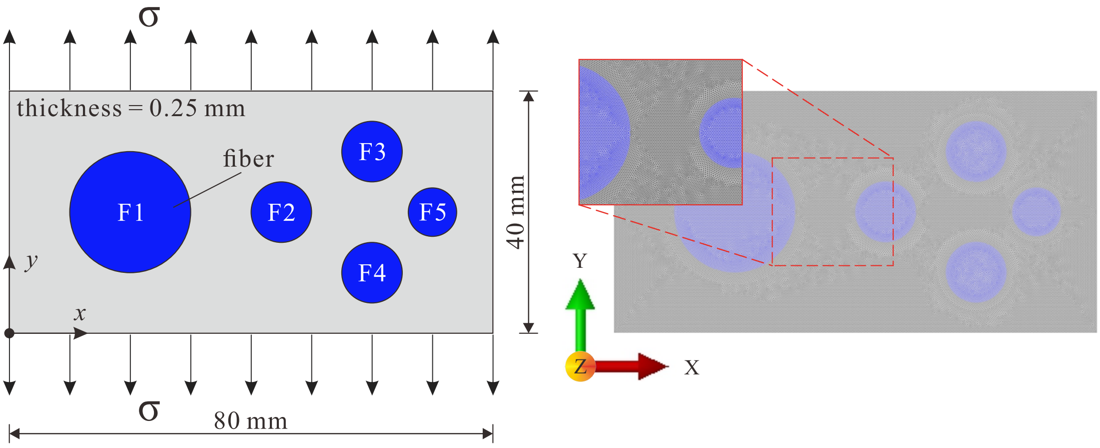

Figure 14: 3D rectangular plate with cylindrical fibers: geometry (left) and 3D mesh model (right).

The material properties are shown in Table 1, and the cohesive parameters for model I as shown in Fig. 2 are used. The numerical simulations are conducted with $\Delta t = 0.2\ \mu s$ in the following. Fig. 15 shows the fracture process at different times. We can observe that cracks nucleate from the interface and then kink into the matrix when reaching a certain point. Subsequently, these interface cracks and matrix cracks are interconnected and then lead to a complex fracture pattern. The evolution of fracture energy and plastic energy is shown in Fig. 16.

Table 1: Material parameters used in the numerical simulations

Name	Symbol	Matrix	Fiber	Unit
Young's modulus	E	32	60	GPa
Poisson's ratio	ν	0.2	0.25	[–]
Mass density	ρ	2450	4750	kg/m^3
Yield stress	σ_y	4	8	MPa
Hardening modulus	H	2	4	MPa
Critical fracture stress	σ_c	10	30	MPa

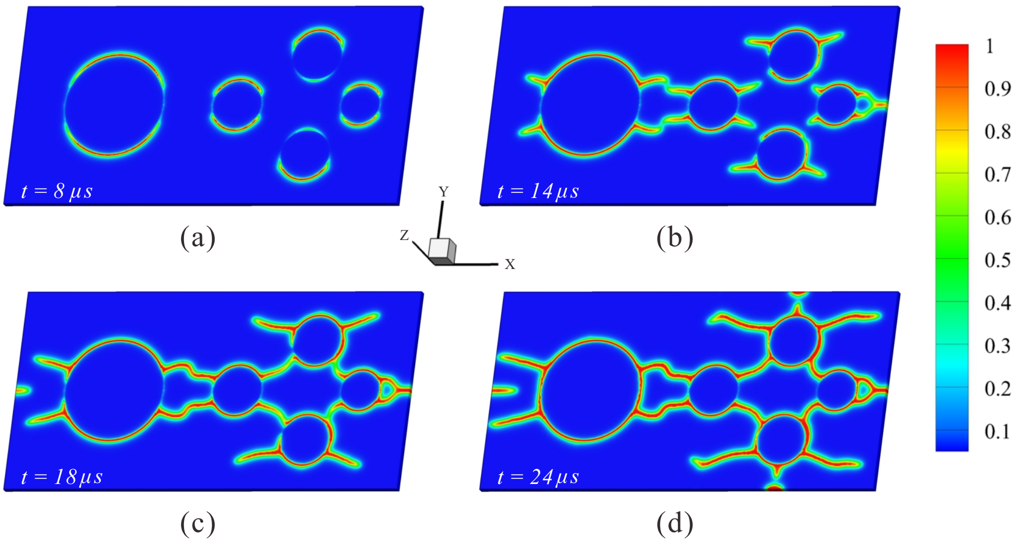

(a) (b) (c) (d)

Figure 15: 3D rectangular plate with cylindrical fibers: crack patterns at (a) $t = 8$ μs, (b) $t = 14$ μs, (c) $t = 18$ μs and (d) $t = 24$ μs.

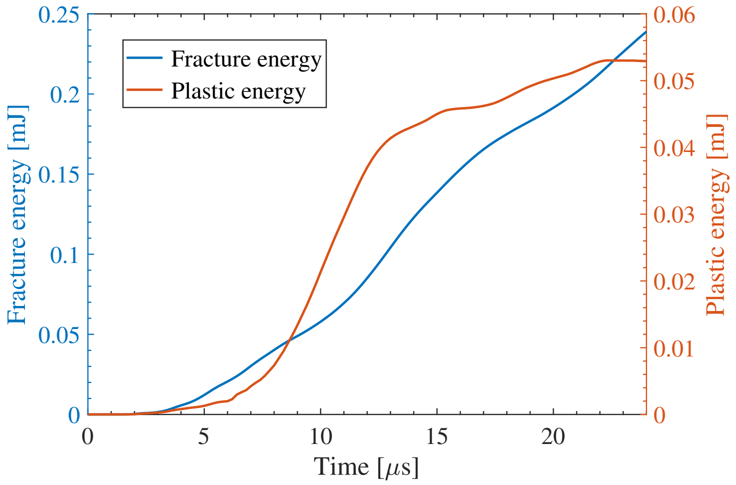

Figure 16: 3D rectangular plate with cylindrical fibers: evolution of fracture energy and plastic energy.

Further, we use this complex structure to further investigate the influence of interface and cohesive parameters. With the similar manner as shown in Section 5.1.2, another two numerical simulations with cohesive model II and no-interface are implemented, respectively. Fig. 17 shows the fracture patterns for the three simulations. We notice that there is not crack initiation until $t = 200$ μs when interfaces are not considered. Fig. 18 shows the comparison of fracture/plastic energy obtained with model I and model II. The results demonstrate again that, interface has an obvious influence on the crack patterns and fracture/plastic energy, while cohesive parameters seem do not have obvious effect on the fracture patterns and fracture/plastic energy when interface is considered.

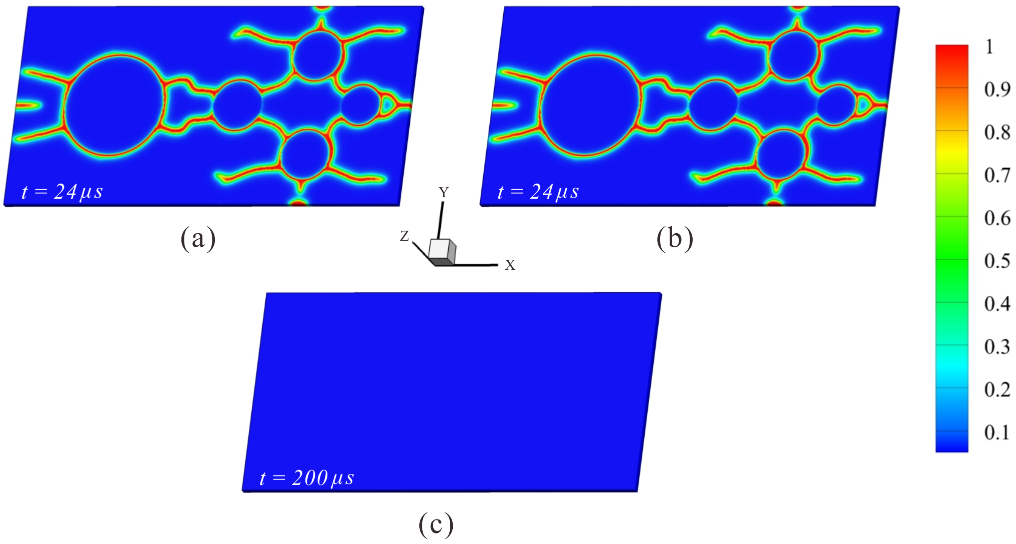

Figure 17: 3D rectangular plate with cylindrical fibers: fracture patterns obtained from (a) model I, (b) model II and (c) no-interface.

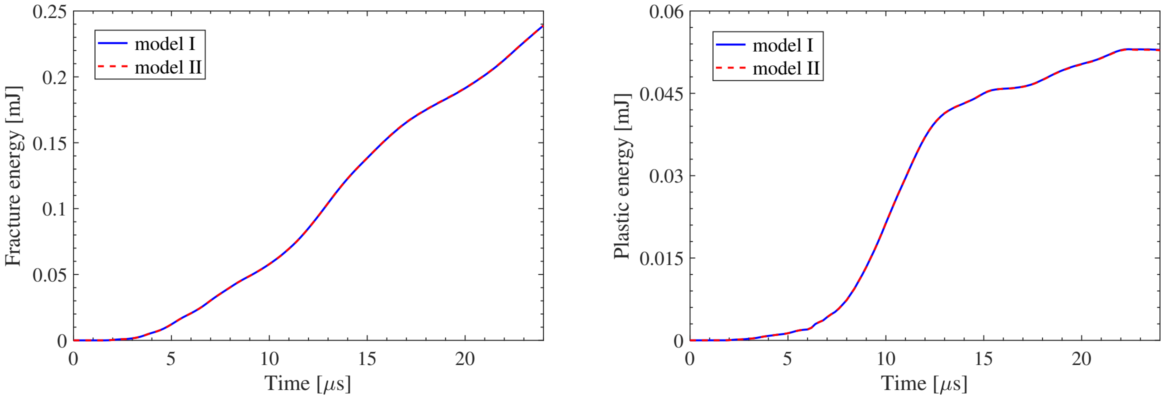

Figure 18: 3D rectangular plate with cylindrical fibers: comparison of fracture energy (left) and plastic energy (right) obtained from model I and model II.

Finally, we further investigated the convergence of the model with respect to the mesh refinement. For this purpose, the previous simulation is conducted with another two refined meshes with 247364 elements and 485672 elements, respectively. Fig. 19 shows the final fracture patterns for the three mesh models. Fig. 20 shows the fracture/plastic energy for the three mesh models. The results illustrate again the convergence of the method with mesh refinement.

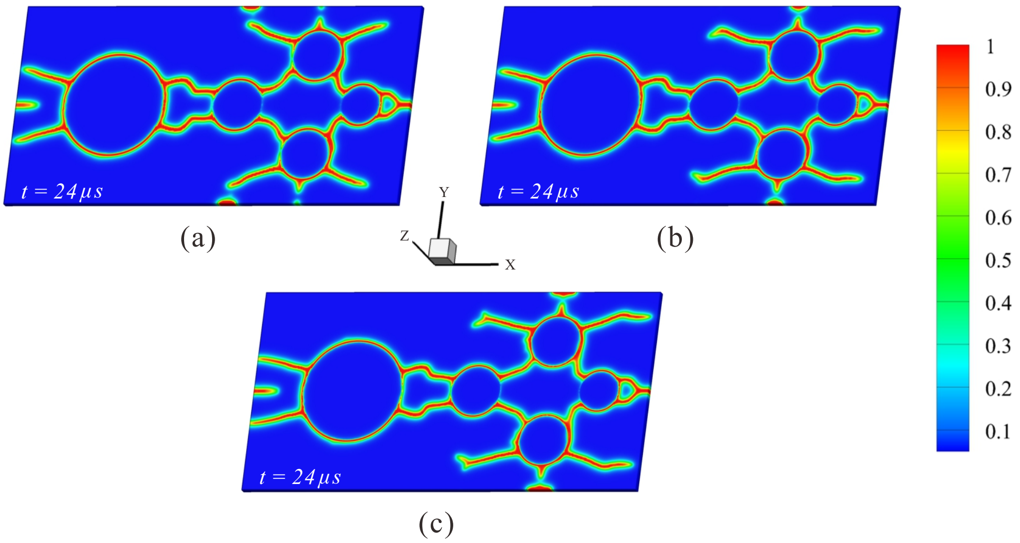
(a) (b) (c)

Figure 19: 3D rectangular plate with cylindrical fibers. The final fracture patterns for (a) mesh 1 (247364 elements), (b) mesh 2 (356938 elements) and (c) mesh 3 (485672 elements).

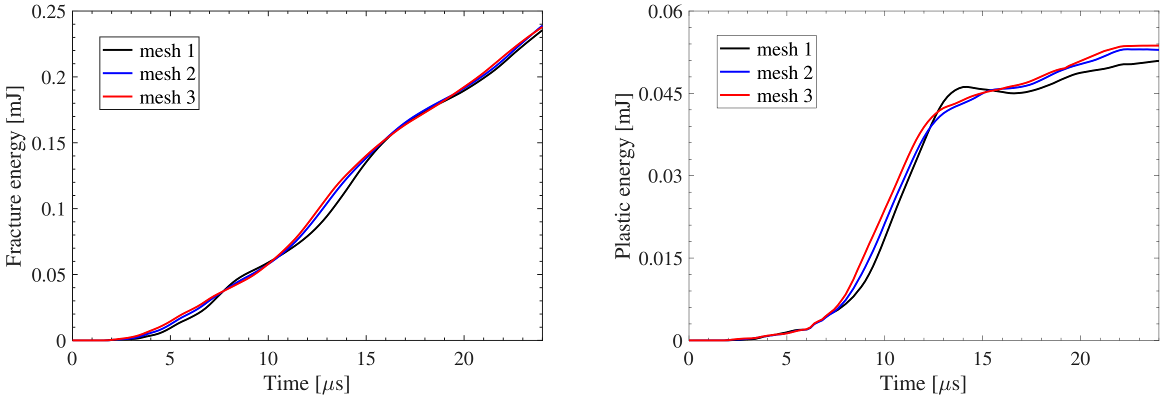

Figure 20: 3D rectangular plate with cylindrical fibers. The fracture energy (left) and plastic energy (right) for mesh 1 (247364 elements), mesh 2 (356938 elements) and mesh 3 (485672 elements).

5.3. 3D complex microstructure obtained from microtomography

In this example, we investigate the capabilities of the proposed method to simulate microcrack propagation in 3D complex microstructure obtained from microtomography such as obtained by experimental imaging techniques, like X-ray computed tomography (XRCT) technique. The microstructure is extracted from a 3D printed fiber reinforced elastoplastic composite sample and has the dimensions $0.178 \times 0.178 \times 0.178$ mm^3, as shown in Fig. 21a. The spatial discretization of the 3D microstructure comprises 709105 tetrahedral elements (see Fig. 21b) with the minimal element size $h_e = 0.002$ mm, where pore phases are not meshed to save the computational costs.

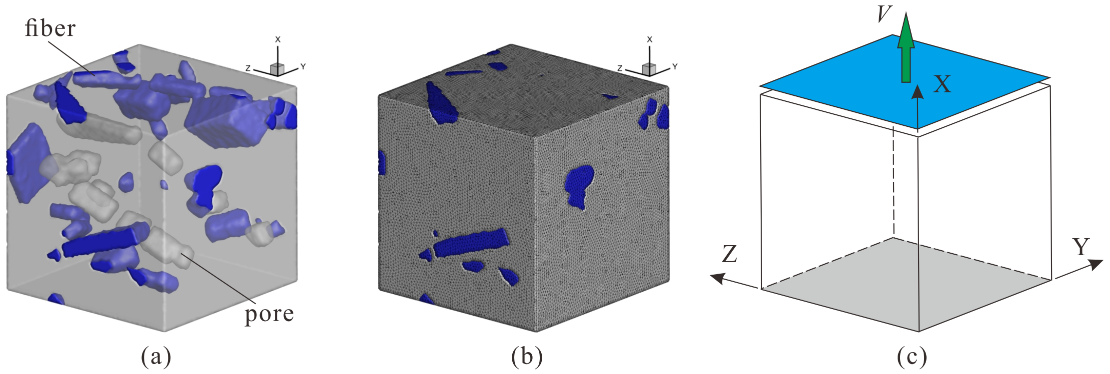

Figure 21: 3D complex microstructure obtained from microtomography: (a) whole microstructure model (size: $0.178 \times 0.178 \times 0.178$ mm^3), (b) mesh model and (c) boundary conditions.

The material parameters are shown in Table 1, and the cohesive parameters for model I as shown in Fig. 2 are used. The boundary conditions are as follows (see Fig. 21c): on the lower end ($x = 0$), the (x, y, z)-components are fixed, on the upper end, the (y, z)-components are free, while the x-velocities are prescribed by

$$v(t) = \begin{cases} \frac{v_1}{t_0} t & \text{if } \; t \leq t_0 \\ v_1 & \text{otherwise} \end{cases} \tag{78}$$

for $t_0 = 0.02$ μs and $v_1 = 100$ mm/s. The numerical simulations are conducted with $\Delta t = 0.01$ μs and named as "x-loading" in the following.

Fig. 22 shows the fracture process at different times, where for the sake of clear visualization, only the crack phase field with values higher than 0.9 is plotted. As can be seen, cracks are initiated in the form of interface debonding and then migrate into the matrix in the form of matrix cracks. Subsequently, these interface cracks and matrix cracks are connected and then lead to the final failure of the microstructure. The similar damage phenomena can also be found in Section 5.2. The evolution of fracture energy and plastic energy is shown in Fig. 23.

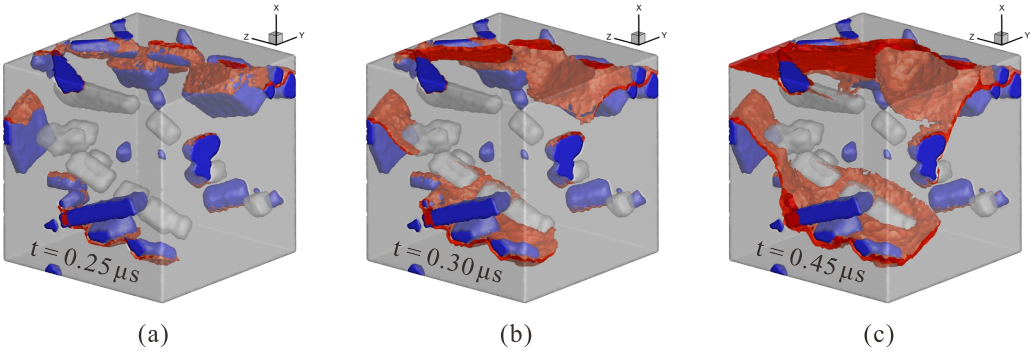

Figure 22: 3D complex microstructure obtained from microtomography: crack patterns at (a) $t = 0.25$ μs, (b) $t = 0.30$ μs and (c) $t = 0.45$ μs. For the sake of clear visualization, only the crack phase field with values higher than 0.9 is plotted.

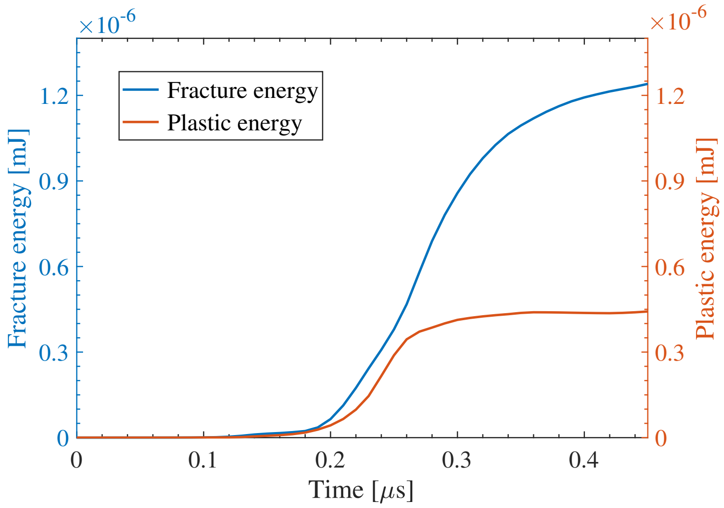

Figure 23: 3D complex microstructure obtained from microtomography: evolution of fracture energy and plastic energy.

Finally, we investigate the capabilities of the proposed method to qualitatively capture the anisotropic behavior of 3D printed microstructure. For this purpose, two additional simulations are performed: (i) in the first one, called "y-loading", the boundary conditions are as follows: on the plane $y = 0$, the (x, y, z)-components are fixed, on the plane $y = \max(y)$, the (x, z)-components are free, while the y-velocities are prescribed by (78), and (ii) in the second one, called "z-loading", the (x, y, z)-components are fixed on the plane $z = 0$, on the plane $z = \max(z)$, the (x, y)-components are free, while the z-velocities are prescribed by (78). Fig. 24 shows the final fracture patterns for the three simulations. Fig. 25 shows the comparison of fracture energy and plastic energy. The results show an obvious difference and demonstrate the capabilities of the proposed method to qualitatively capture the anisotropic behavior of 3D printed microstructure.

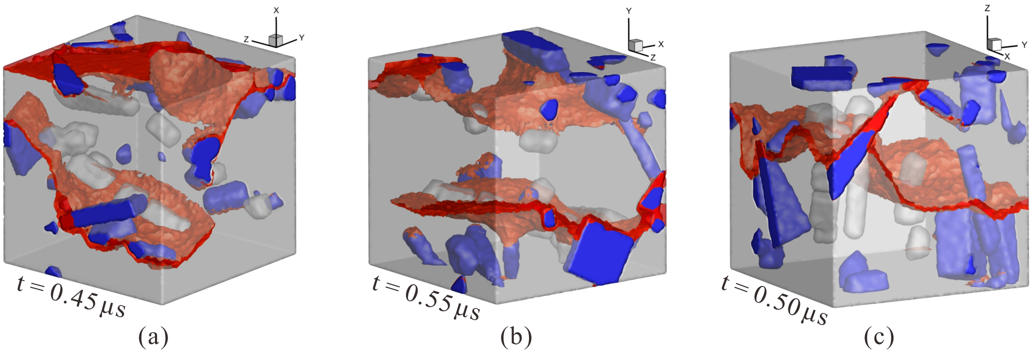

(a) (b) (c)

Figure 24: 3D complex microstructure obtained from microtomography: final fracture patterns for (a) x-loading, (b) y-loading and (c) z-loading. For the sake of clear visualization, only the crack phase field with values higher than 0.9 is plotted.

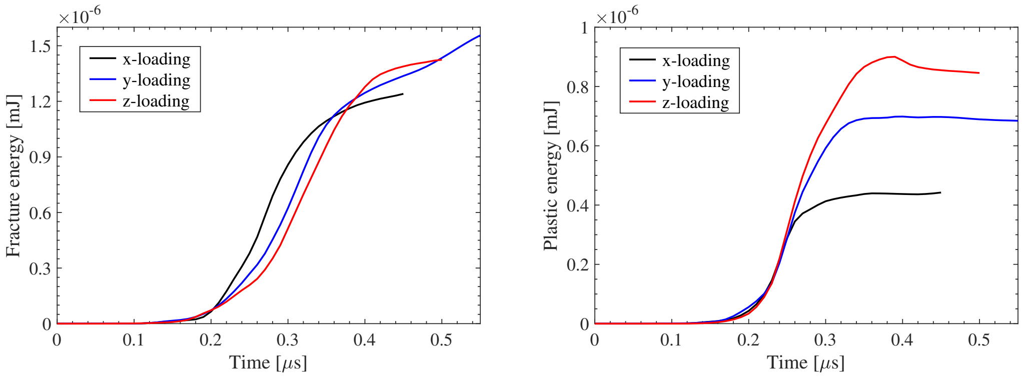

Figure 25: 3D complex microstructure obtained from microtomography: comparison of fracture energy (left) and plastic energy (right) for three different loading directions.

6. Conclusion

In this work, we have extended a dynamic phase field model based on the work [44], to take into account the following features: (i) interfacial debonding in the elastoplastic composites; (ii) interactions between interfacial debonding and bulk dynamic ductile fracture; (iii) the possibility to handle elastoplastic composite microstructures obtained from X-ray computed tomography (XRCT) technique. In order to consider interfacial damage, the total energy has been modified by adding a strain density depending on the displacement jump, where interfaces are regularized by a length scale parameter and singular strain part along the interfaces is approximated by using a Taylor expansion. In that manner, different damage mechanisms can be associated with interfaces as compared to the matrix cracking mechanisms. Different equations (displacement, plasticity and damage) can be obtained by using the variational principle and then be solved in a staggered iterative procedure. As a result, this extension allows simulating initiation, propagation and interactions between both bulk dynamic fracture and interfacial debonding in elastoplastic composites without specific treatment and use of classical finite elements. Several numerical examples, involving complex microstructures e.g. obtained from 3D printed short fiber reinforced composites, have shown the capability of the method to handle complex micro cracks interactions for arbitrary complexity of the microstructures, and the convergence with respect to the mesh refinement. To our best knowledge, the presented simulations involving ductile dynamic fracturing, considering interfacial debonding and realistic microstructure directly obtaining from an experimental XRCT have been presented here for the first time. Then, the present model seems to be very promising for predicting initiation, propagation of complex microcracking in a dynamic-mechanical context in elastoplastic composites, such as 3D printed fiber reinforced composites used in aerospace. One future perspective of this work would be extended to adaptive mesh refinement to deal with the high computaional cost causing by the use of a large number of elements in undamaged zones.

Acknowledgements

Pengfei Li gratefully acknowledges the financial support from Jiangsu Open University Fourteenth Five-Year Plan Project with project number 2022XK008 and from Jiangsu Education Department with project number 23KJB130002. Yi Wu acknowledges support from the China Postdoctoral Science Foundation (Grant No. 2023M730217). This work has also benefited from the project ”Multiscale Modeling and Experimental Investigation of damage in composite components obtained by additive manufacturing process” (MMELED), ANR-16-CE08-0044-04.

Conflict of interest statement

On behalf of all authors, the corresponding author states that there is no conflict of interest.

References

[1] D. Yavas, Z. Zhang, Q. Liu, D. Wu, Fracture behavior of 3d printed carbon fiber-reinforced polymer composites, Composites Science and Technology 208 (2021) 108741.

[2] M. N. Islam, K. P. Baxevanakis, V. V. Silberschmidt, Dynamic fracture behaviour of additively manufactured polymers and composites under ballistic impact, Procedia Structural Integrity 37 (2022) 217–224.

[3] I. Iturrioz, L. F. F. Miguel, J. D. Riera, Dynamic fracture analysis of concrete or rock plates by means of the discrete element method, Latin American journal of solids and structures 6 (3) (2009) 229Â–245.

[4] L. F. Orozco, J.-Y. Delenne, P. Sornay, F. Radjai, Discrete-element model for dynamic fracture of a single particle, International Journal of Solids and Structures 166 (2019) 47–56.

[5] Y. D. Ha, F. Bobaru, Studies of dynamic crack propagation and crack branching with peridynamics, International Journal of Fracture 162 (2010) 229–244.

[6] B. Kilic, E. Madenci, An adaptive dynamic relaxation method for quasi-static simulations using the peridynamic theory, Theoretical and Applied Fracture Mechanics 53 (3) (2010) 194–204.

[7] W. Hu, Y. D. Ha, F. Bobaru, Peridynamic model for dynamic fracture in unidirectional fiber-reinforced composites, Computer Methods in Applied Mechanics and Engineering 217 (2012) 247–261.

[8] X.-P. Xu, A. Needleman, Numerical simulations of fast crack growth in brittle solids, Journal of the Mechanics and Physics of Solids 42 (9) (1994) 1397–1434.

[9] J. Ožbolt, J. Bošnjak, E. Sola, Dynamic fracture of concrete compact tension specimen: Experimental and numerical study, International Journal of Solids and Structures 50 (25-26) (2013) 4270–4278.

[10] C. Wolff, N. Richart, J.-F. Molinari, A non-local continuum damage approach to model dynamic crack branching, International Journal for Numerical Methods in Engineering 101 (12) (2015) 933–949.

[11] T. Belytschko, H. Chen, J. Xu, G. Zi, Dynamic crack propagation based on loss of hyperbolicity and a new discontinuous enrichment, International journal for numerical methods in engineering 58 (12) (2003) 1873–1905.

[12] A. Combescure, A. Gravouil, D. Grégoire, J. Réthoré, X-fem a good candidate for energy conservation in simulation of brittle dynamic crack propagation, Computer Methods in Applied Mechanics and Engineering 197 (5) (2008) 309–318.

[13] H. Nguyen-Vinh, I. Bakar, M. A. Msekh, J.-H. Song, J. Muthu, G. Zi, P. Le, S. P. A. Bordas, R. Simpson, S. Natarajan, et al., Extended finite element method for dynamic fracture of piezo-electric materials, Engineering Fracture Mechanics 92 (2012) 19–31.

[14] E. Chen, Continuum damage mechanics studies on the dynamic fracture of concrete, MRS Online Proceedings Library 64 (1) (1985) 63–77.

[15] I. Lee, Y. Ochi, S. Bae, J. Song, Continuum damage modeling for dynamic fracture toughness of metal matrix composites, Journal of Solid Mechanics and Materials Engineering 3 (7) (2009) 931–942.

[16] G. A. Francfort, J.-J. Marigo, Revisiting brittle fracture as an energy minimization problem, Journal of the Mechanics and Physics of Solids 46 (8) (1998) 1319–1342.

[17] H. Amor, J.-J. Marigo, C. Maurini, Regularized formulation of the variational brittle fracture with unilateral contact: Numerical experiments, Journal of the Mechanics and Physics of Solids 57 (8) (2009) 1209–1229.

[18] C. Miehe, M. Hofacker, F. Welschinger, A phase field model for rate-independent crack propagation: Robust algorithmic implementation based on operator splits, Computer Methods in Applied Mechanics and Engineering 199 (45-48) (2010) 2765–2778.

[19] M. J. Borden, C. V. Verhoosel, M. A. Scott, T. J. Hughes, C. M. Landis, A phase-field description of dynamic brittle fracture, Computer Methods in Applied Mechanics and Engineering 217 (2012) 77–95.

[20] M. Ambati, T. Gerasimov, L. De Lorenzis, A review on phase-field models of brittle fracture and a new fast hybrid formulation, Computational Mechanics 55 (2015) 383–405.

[21] J.-Y. Wu, A unified phase-field theory for the mechanics of damage and quasi-brittle failure, Journal of the Mechanics and Physics of Solids 103 (2017) 72–99.

[22] J.-Y. Wu, V. P. Nguyen, C. T. Nguyen, D. Sutula, S. Sinaie, S. P. Bordas, Phase-field modeling of fracture, Advances in applied mechanics 53 (2020) 1–183.

[23] M. Ambati, T. Gerasimov, L. De Lorenzis, Phase-field modeling of ductile fracture, Computational Mechanics 55 (2015) 1017–1040.

[24] B. Yin, M. Kaliske, A ductile phase-field model based on degrading the fracture toughness: Theory and implementation at small strain, Computer Methods in Applied Mechanics and Engineering 366 (2020) 113068.

[25] M. Ambati, R. Kruse, L. De Lorenzis, A phase-field model for ductile fracture at finite strains and its experimental verification, Computational Mechanics 57 (2016) 149–167.

[26] R. Alessi, J.-J. Marigo, S. Vidoli, Gradient damage models coupled with plasticity: variational formulation and main properties, Mechanics of Materials 80 (2015) 351–367.

[27] M. J. Borden, T. J. Hughes, C. M. Landis, A. Anvari, I. J. Lee, A phase-field formulation for fracture in ductile materials: Finite deformation balance law derivation, plastic degradation, and stress triaxiality effects, Computer Methods in Applied Mechanics and Engineering 312 (2016) 130–166.

[28] C. Kuhn, T. Noll, R. Müller, On phase field modeling of ductile fracture, GAMM-Mitteilungen 39 (1) (2016) 35–54.

[29] T. You, Q.-Z. Zhu, P.-F. Li, J.-F. Shao, Incorporation of tension-compression asymmetry into plastic damage phase-field modeling of quasi brittle geomaterials, International Journal of Plasticity 124 (2020) 71–95.

[30] C. Miehe, F. Aldakheel, A. Raina, Phase field modeling of ductile fracture at finite strains: A variational gradient-extended plasticity-damage theory, International Journal of Plasticity 84 (2016) 1–32.

[31] C. Miehe, F. Aldakheel, S. Teichtmeister, Phase-field modeling of ductile fracture at finite strains: A robust variational-based numerical implementation of a gradient-extended theory by micromorphic regularization, International Journal for Numerical Methods in Engineering 111 (9) (2017) 816–863.

[32] M. Dittmann, F. Aldakheel, J. Schulte, P. Wriggers, C. Hesch, Variational phase-field formulation of non-linear ductile fracture, Computer Methods in Applied Mechanics and Engineering 342 (2018) 71–94.

[33] C. Samaniego, J. Ulloa, P. Rodríguez, G. Houzeaux, M. Vázquez, E. Samaniego, A phase-field model for ductile fracture with shear bands: A parallel implementation, International Journal of Mechanical Sciences 200 (2021) 106424.

[34] R. Alessi, M. Ambati, T. Gerasimov, S. Vidoli, L. De Lorenzis, Comparison of phase-field models of fracture coupled with plasticity, Advances in computational plasticity: A book in honour of D. Roger J. Owen (2018) 1–21.

[35] C. J. Larsen, C. Ortner, E. Süli, Existence of solutions to a regularized model of dynamic fracture, Mathematical Models and Methods in Applied Sciences 20 (07) (2010) 1021–1048.

[36] B. Bourdin, C. J. Larsen, C. L. Richardson, A time-discrete model for dynamic fracture based on crack regularization, International journal of fracture 168 (2011) 133–143.

[37] M. Hofacker, C. Miehe, A phase field model of dynamic fracture: Robust field updates for the analysis of complex crack patterns, International Journal for Numerical Methods in Engineering 93 (3) (2013) 276–301.

[38] J. Bleyer, C. Roux-Langlois, J.-F. Molinari, Dynamic crack propagation with a variational phase-field model: limiting speed, crack branching and velocity-toughening mechanisms, International Journal of Fracture 204 (1) (2017) 79–100.

[39] V. P. Nguyen, J.-Y. Wu, Modeling dynamic fracture of solids with a phase-field regularized cohesive zone model, Computer Methods in Applied Mechanics and Engineering 340 (2018) 1000–1022.

[40] Y. Liu, Y. Feng, D. Wu, X. Chen, W. Gao, Virtual modelling integrated phase field method for dynamic fracture analysis, International Journal of Mechanical Sciences 252 (2023) 108372.

[41] R. J. Geelen, Y. Liu, T. Hu, M. R. Tupek, J. E. Dolbow, A phase-field formulation for dynamic cohesive fracture, Computer Methods in Applied Mechanics and Engineering 348 (2019) 680–711.

[42] J. Bleyer, J.-F. Molinari, Microbranching instability in phase-field modelling of dynamic brittle fracture, Applied Physics Letters 110 (15) (2017).

[43] C. Miehe, M. Hofacker, L.-M. Schänzel, F. Aldakheel, Phase field modeling of fracture in multi-physics problems. part ii. coupled brittle-to-ductile failure criteria and crack propagation in thermo-elastic–plastic solids, Computer Methods in Applied Mechanics and Engineering 294 (2015) 486–522.

[44] G. Molnár, A. Gravouil, R. Seghir, J. Réthoré, An open-source abaqus implementation of the phase-field method to study the effect of plasticity on the instantaneous fracture toughness in dynamic crack propagation, Computer Methods in Applied Mechanics and Engineering 365 (2020) 113004.

[45] L. Wu, Q. Shen, An elastoplastic phase-field model for dynamic fracture of nickel-base super-alloys, International Journal of Solids and Structures (2023) 112432.

[46] M. Paggi, J. Reinoso, Revisiting the problem of a crack impinging on an interface: a modeling framework for

the interaction between the phase field approach for brittle fracture and the interface cohesive zone model, Computer Methods in Applied Mechanics and Engineering 321 (2017) 145–172.

[47] M. A. Msekh, M. Silani, M. Jamshidian, P. Areias, X. Zhuang, G. Zi, P. He, T. Rabczuk, Predictions of j integral and tensile strength of clay/epoxy nanocomposites material using phase field model, Composites Part B: Engineering 93 (2016) 97–114.

[48] M. A. Msekh, N. Cuong, G. Zi, P. Areias, X. Zhuang, T. Rabczuk, Fracture properties prediction of clay/epoxy nanocomposites with interphase zones using a phase field model, Engineering Fracture Mechanics 188 (2018) 287–299.

[49] A. C. Hansen-Dörr, R. de Borst, P. Hennig, M. Kästner, Phase-field modelling of interface failure in brittle materials, Computer Methods in Applied Mechanics and Engineering 346 (2019) 25–42.

[50] T. T. Nguyen, J. Yvonnet, Q.-Z. Zhu, M. Bornert, C. Chateau, A phase-field method for computational modeling of interfacial damage interacting with crack propagation in realistic microstructures obtained by microtomography, Computer Methods in Applied Mechanics and Engineering 312 (2016) 567–595.

[51] T. Nguyen, J. Yvonnet, D. Waldmann, Q.-C. He, Phase field modeling of interfacial damage in heterogeneous media with stiff and soft interphases, Engineering Fracture Mechanics 218 (2019) 106574.

[52] L. Ambrosio, V. M. Tortorelli, Approximation of functional depending on jumps by elliptic functional via t-convergence, Communications on Pure and Applied Mathematics 43 (8) (1990) 999–1036.

[53] M. Van den Bosch, P. Schreurs, M. Geers, An improved description of the exponential xu and needleman cohesive zone law for mixed-mode decohesion, Engineering Fracture Mechanics 73 (9) (2006) 1220–1234.

[54] T. T. Nguyen, J. Yvonnet, M. Bornert, C. Chateau, K. Sab, R. Romani, R. Le Roy, On the choice of parameters in the phase field method for simulating crack initiation with experimental validation, International Journal of Fracture 197 (2) (2016) 213–226.

[55] X. Zhang, C. Vignes, S. W. Sloan, D. Sheng, Numerical evaluation of the phase-field model for brittle fracture with emphasis on the length scale, Computational Mechanics 59 (2017) 737–752.

[56] J.-Y. Wu, V. P. Nguyen, A length scale insensitive phase-field damage model for brittle fracture, Journal of the Mechanics and Physics of Solids 119 (2018) 20–42.

[57] M. Frémond, B. Nedjar, Damage, gradient of damage and principle of virtual power, International journal of solids and structures 33 (8) (1996) 1083–1103.

[58] P. Rodriguez, J. Ulloa, C. Samaniego, E. Samaniego, A variational approach to the phase field modeling of brittle and ductile fracture, International Journal of Mechanical Sciences 144 (2018) 502–517.

[59] P. Li, J. Yvonnet, C. Combescure, H. Makich, M. Nouari, Anisotropic elastoplastic phase field fracture modeling of 3d printed materials, Computer Methods in Applied Mechanics and Engineering 386 (2021) 114086.

[60] A. Mielke, Evolution of rate-independent systems, Evolutionary equations 2 (2005) 461–559.

[61] K. Pham, J.-J. Marigo, C. Maurini, The issues of the uniqueness and the stability of the homogeneous response in uniaxial tests with gradient damage models, Journal of the Mechanics and Physics of Solids 59 (6) (2011) 1163–1190.

[62] P. Li, J. Yvonnet, C. Combescure, An extension of the phase field method to model interactions between interfacial damage and brittle fracture in elastoplastic composites, International Journal of Mechanical Sciences 179 (2020) 105633.